FRESH WATER ICE

VISIBLE/INFRARED IMAGER/RADIOMETER SUITE ALGORITHM THEORETICAL BASIS DOCUMENT

Version 3: May 2000

Igor Appel
Ken Jensen

EDR: FRESH WATER ICE

Doc No: Y2404

Version: 3

Revision: 0

	Function	Name	Signature	Date
Prepared by	EDR Developer	I. APPEL		
Approved by	Relevant IPT Lead	K. JENSEN		
Approved by	Chief Scientist	P. ARDANUY		
Released by	Program Manager	H. BLOOM		

TABLE OF CONTENTS

Raytheon

LIST OF FIGURES

LIST OF TABLES

GLOSSARY OF ACRONYMS

AMSR	Advanced Microwave Scanning Radiometer
ARM	Atmospheric Radiation Measurements
ATBD	Algorithm Theoretical Basis Document
AVHRR	Advanced Very High Resolution Radiometer
BRDF	Bidirectional Reflectance Distribution Function
CMIS	Conical-Scanning Microwave Imager/Sounder
EDR	Environmental Data Record
ERS	European Remote Sensing Satellite
FIRE-ACE	First ISCCP Regional Experiment-Arctic Cloud Experiment
GIFOV	Ground Imaged Field of View
GLERL	Great Lakes Environmental Research Laboratory
ISCCP	International Satellite Cloud Climatology Project
LUT	Look-Up Table
MAS	MODIS Airborne Simulator
MESMA	Multiple Endmember Spectral Mixture Analysis
MODIS	Moderate Resolution Imaging Spectroradiometer
NOAA	National Oceanographic and Atmospheric Administration
NPOESS	National Polar-orbiting Operational Environmental Satellite System
NPP	NPOESS Preparatory Program
RMS	Root Mean Squared
RMSE	Root Mean Squared Error
SAR	Synthetic Aperture Radar
SBRS	Santa Barbara Remote Sensing
SDR	Sensor Data Record
SHEBA	Surface Heat Budget of the Arctic Ocean
SMA	Spectral Mixture Analysis
SRD	Sensor Requirements Document
TOA	Top of Atmosphere
VHRR	Very High Resolution Radiometer
VIIRS	Visible/Infrared Imager/Radiometer Suite
VIR	Visible-Infrared
VSCA	VIIRS Snow Cover Algorithm

ABSTRACT

This Fresh Water Ice Algorithm Theoretical Basis Document describes the background, theory, and analysis an algorithmic approach that can be used to develop operational algorithms to retrieve fresh water ice concentration and fresh water ice edge boundary automatically from Visible-Infrared remote sensing data. The data will be in the form of Sensor Data Records (SDRs) produced by the National Polar-Orbiting Operational Environment Satellite System (NPOESS) the Visible/Infrared Imager/Radiometer Suite (VIIRS). Fully automated retrievals of fresh water ice data from Vis-IR will be of great value to operational ice centers in the NPOESS era.

Our process to create Fresh Water Ice Environmental Data Records (EDRs) from the VIIRS data has been developed to satisfy the requirements of VIIRS Sensor Requirements Document (SRD), Version Two, Revision a. This document is version 3 of the Fresh Water Ice ATBD. It is intended to completely supersede previous versions.

The VIIRS Fresh Water Ice EDR requires that fresh water ice concentration be retrieved at a regional horizontal cell size of 2 km at nadir under clear conditions. A measurement range from 0.1 to 1.0 is required, with a measurement uncertainty of 0.1. Ice edge boundary location is required, with a measurement uncertainty of 10 km. The horizontal coverage will include all fresh water bodies with a minimum size of 10 km in all directions.

Fresh water ice concentration is defined as the fraction of a given area of fresh water that is covered by ice. Ice concentration is reported as a gridded product for areas of size limited by the Horizontal Cell Size (HCS) requirement and separation limited by the Horizontal Reporting Interval requirement.

Ice edge boundary is defined as the contour separating fresh water from fresh water ice. Following the SRD definition of sea ice edge location, the fresh water ice edge is defined as the boundary between ice concentration > 0.1 and ice concentration ≤ 0.1.

The algorithms of ice concentration and ice edge boundary retrieval have changed since the version 2 ATBD.

We retrieve ice concentration from an automated algorithm. The algorithm includes the derivation of ice fraction for fine resolution pixels, using tie point analysis of ice surface temperature and/or surface reflectances. Operational capability is achieved by the use of local search windows to derive ice and water tie points. Ice concentration is retrieved as a gridded product at fine resolution with measurement uncertainty better than 0.1 in most cases.

An automated algorithm produces ice edge location as a contour on a map (an ice edge image, or "isoline") and also as a set of latitude/longitude coordinates. The coordinates are determined at subpixel resolution by interpolation of the ice concentration map in the vicinity of the ice edge isoline. A compact ice edge boundary is located in most cases with a measurement uncertainty of less than 0.3 km at nadir. The ice edge location and ice concentration retrieved by our automated algorithms will be archived as a part of the VIIRS Fresh Water Ice EDR product, for use by analysts at national ice centers.

Optimized parameters of a search window and band weight reduce tie point errors and provide a seamless day/night transition.

This document presents the algorithm theoretical basis, the input data requirements, the EDR performance specification and error analysis, conditions under which the specification can not be attained, and the plan for initialization and validation. It is a substantial revision of our version 2 algorithm, which should be considered to be completely superseded by the new version.

1.0 INTRODUCTION

1.1 PURPOSE

This Algorithm Theoretical Basis Document (ATBD) explains the mathematical background to derive the Fresh Water Ice Environmental Data Record (EDR). In addition, this document provides an overview of the required input data, physical theory, assumptions, limitations, and a performance analysis of the described algorithm. The Fresh Water Ice EDR is obtained from measurements of the National Polar-orbiting Operational Environmental Satellite System (NPOESS) Visible/Infrared Imager/Radiometer Suite (VIIRS). The one EDR described in this document is part of the NPOESS/VIIRS team software package of a total of 29 EDRs.

1.2 SCOPE

This section of the ATBD introduces the algorithm. Section 2 provides an overview of the EDR requirements, specifications, and retrieval strategy. Section 3 describes the algorithm's functions in detail, including the theoretical basis, mathematical description, and performance analysis. Section 4 states the assumption and limitations on which the algorithm is based, and Section 5 provides references for the publications cited in this document.

1.3 VIIRS DOCUMENTS

This document contains references to other VIIRS documents, shown in italicized brackets. The VIIRS documents cited in this document are:

[SS 154640-001]	VIIRS System Specification
[Y2466]	Imagery ATBD
[Y2401]	Snow Cover/Depth ATBD
[Y2405]	Ice Surface Temperature ATBD
[Y2409]	Sea Ice Age/Edge Motion ATBD
[Y2411]	Atmospheric Correction Over Land ATBD
[Y2412]	Cloud Mask ATBD
[Y2477]	Snow/Ice Module Software Architecture
[Y3258]	Earth Location ATBD
[Y3261]	RDR to SDR Conversion ATBD
[Y4963]	VIIRS Imagery TIM, March 8, 2000

1.4 REVISIONS

This is the third version of this document, dated May 2000. The first two versions were developed in response to VIIRS Sensor Requirements Document (SRD), revision 1, dated August 3, 1998. The first version was dated October 1998. The second version was dated June

1999. The third version has been developed in response to VIIRS Sensor Requirements Document (SRD), Version 2, Revision a, dated 04 November 1999.

Changes since version 2 are largely in response to revisions in the new SRD. They include:

- Modification of the process flow

- Development of scene-specific tie point analysis of reflectance and/or surface temperature for the automated ice concentration algorithm

- Development of an automated algorithm to retrieve ice edge boundary location

- Reporting of ice edge boundary as an ice edge map and a set of latitude/longitude coordinates

- Additional test results, from an expanded test data set

- A revised specification, with supporting error analysis and error budget

2.0   EXPERIMENT OVERVIEW

2.1   OBJECTIVES OF THE FRESH WATER ICE RETRIEVAL

Fresh water ice concentration is defined as the fraction of a given area of fresh water that is covered by ice, quantized to the nearest one tenth. Ice edge boundary is the contour separating fresh water from fresh water ice. The requirements (Table 1) apply only under clear conditions.

Table 1. Specifications of the VIIRS Fresh Water Ice EDR

Units: Concentration: Dimensionless
          Ice Edge Boundary: lat/long

Para. No.		Thresholds	Objectives	Specification Value
	a. Horizontal Cell Size			
V40.7.2-1	1. At nadir	2 km (TBR)	(TBD)	0.8 km
V40.7.2-2	2. Worst case	3.2 km (TBR)	2.6 km	3.2 km
V40.7.2-3	b. Horizontal Reporting Interval	Horizontal Cell Size (TBD)	Horizontal Cell Size (TBD)	Horizontal Cell Size
V40.7.2-4	c. Horizontal Coverage	Fresh Water	Fresh Water	Fresh Water
V40.7.2-5	d. Measurement Range	1/10 to 10/10 concentration, 1/10 increments	0/10 to 10/10 concentration, 1/10 increments	0 - 1 concentration, any value
	e. Measurement Uncertainty			
V40.7.2-6	1. Ice Edge Boundary	10 km	5 km	0.4 km (nadir), 1.0 km (worst case)
V40.7.2-7	2. Ice Concentration	1/10 absolute concentration, for any true value	10 % of true value, for any true value	0.1
V40.7.2-8	f. Mapping Uncertainty	3 km	1 km	67 m (nadir), 233 m (worst case)
V40.7.2-9	i. Minimum Swath Width (All other EDR thresholds met)	3000 km (TBR)	(TBD)	3000 km

Regional retrievals of lake ice concentration are important for commercial transportation planning. Because ice conditions on the major commercial inland waterways vary day by day (Assel, 1990), it is important to retrieve this information in an automated, operational environment. Ice floe forecasts made by the National Ice Center affect the safety of vessels in the Great Lakes during winter (Mannen, 1996).

The ice edge boundary is the contour separating fresh water from fresh water ice. The error in ice edge boundary location is defined as the distance between a measured boundary point and the nearest point on the true ice edge boundary. Ice edge boundaries are used for navigational planning, and so must be available in a short time. The value of an automated retrieval is indicated by the fact that changes in lake ice boundaries typically occur on short time scales (Assel, 1990).

The VIIRS Fresh Water Ice EDR requires that fresh water ice concentration be retrieved at a horizontal cell size of 2 km at nadir and 3.2 km at the edge of scan, under clear conditions. The SRD states that fresh water ice concentration and edge are derived from the Imagery EDR. Our approach to retrieve the Fresh Water Ice EDR is similar to the approach used to retrieve the Imagery EDR Sea Ice Data Application-Related Products *[Y2466]*. The fresh water ice concentration measurement range will be from 0.0 to 1.0, with a measurement uncertainty of 0.1 or better. The EDR also requires the ice edge boundary to be located with a measurement uncertainty of 10 km.

The specifications for fresh water ice will be met by a daytime retrieval algorithm based upon data in reflectance bands, using the surface reflectance properties of snow and ice versus open water. Nighttime retrievals will be made from surface temperature contrast between snow/ice and water.

2.2 HERITAGE

2.2.1 The Great Lakes

The Great Lakes region is, by far, the best-studied area for fresh water ice. The accessibility of the region provides opportunities for extensive *in situ* study, as well as for generating a demand for ice cover data. Information from ice cover data can be useful for solving problems in winter navigation, shoreline engineering, hydropower generation, water supply, and water quality. In addition, a database of Great Lakes ice studies extends back to the previous century, allowing for long-term climate change analysis.

Each Great Lake possesses its own set of characteristics, both physical (volume, shore length, etc.) and hydrometeorological (temperature, precipitation, evaporation patterns, etc.). During a normal winter, ice cover varies from 15 percent on Lake Ontario to 95 percent on Lake Erie. During a severe winter, ice cover on all of the lakes can approach 100 percent (Rondy, 1976).

The Great Lakes Environmental Research Laboratory (GLERL), operated by the National Oceanic and Atmospheric Administration (NOAA), has been responsible for an extensive study of ice on the Great Lakes. Starting in the mid-1970s, a series of studies explored techniques and algorithms to classify and map freshwater ice cover. These studies used Landsat, AVHRR, and European Remote Sensing Satellite (ERS-1) Synthetic Aperature Radar (SAR) data, as well as field studies. The goal of much of this work is to develop an automated method to classify and map Great Lakes ice cover using satellite imagery (Leshkevich, 1995).

Early work for the study, done by visual interpretation of remotely sensed data (Schertler et al., 1975), showed that a variety of ice types and conditions would pose a challenge to automated methods. Each of the ice types common to the Great Lakes is unique in appearance, mode of formation, and physical characteristics. Bolsenga (1983) studied variations in the spectral reflectance of new snow, melting snow, refrozen slush ice, brash ice, pancake ice, and slush curd ice at Great Lakes ground sites. This study measured albedos varying from 0.1 for clear ice to 0.85 for new snow, with different ice types found in the same vicinity. Leshkevich (1981, 1985) analyzed ice cover on Green Bay from Landsat-1 data. He found that seven ice types could be differentiated, but not easily classified. This pointed to the need for a more comprehensive, well-documented library of signatures representing Great Lakes ice types. Additional complications

are caused by temporal variations on time scales of hours (Bolsenga, 1977). These time variations complicate endmember selection and limit the usefulness of ancillary data that are not contemporaneous. Anisotropic reflectance is another important factor.

The work at NOAA/GLERL illustrates the complex nature of ice conditions on the Great Lakes. The results indicate the need for a comprehensive regional database, which would not have been as apparent from remote sensing data alone.

2.2.2   Remote Sensing of Lake Ice

Ice forms in a variety of fresh water bodies, ranging from large lakes to small ponds, throughout temperate and polar zones. The retrieval of fresh water ice properties from remote sensing data is limited by the achievable horizontal spatial resolution and also by the lack of knowledge of conditions on a global scale.

Most remote sensing studies of lake ice have used sensors in the Visible-Infrared (VIR) range, primarily Landsat, Very High Resolution Radiometer (VHRR), and AVHRR.

Landsat observations were used for a manual classification of ice types in Great Lakes ice cover (Leshkevich, 1985), and to study ice cover in Lake Superior and Lake Erie as part of a long-term climatology study (Assel, 1990). NOAA-4 VHRR imagery was used by Wiesnet (1979) for a detailed study of a season on Lake Erie. A series of VHRR images showed the spatial and temporal variability of surface albedo as ice forms, moves, becomes snow-covered, breaks, and melts, under the influence of highly variable temperature and wind conditions. The NOAA/GLERL studies have also used AVHRR data (Leshkevich, 1995).

2.2.2.1   MODIS

The MODIS fresh water ice product is regional in nature. Ice will be mapped in the Great Lakes, Great Bear Lake, Great Slave Lake, Lake Winnipeg, Lake Athabasca, Lake of the Woods, Lake Sakami, Lake Nipigon, Reindeer Lake, Lake Vanern, Lake Ladoga, Lake Baikal, Lake Peipus, Lake Balkhash, and Onega Lake. The MODIS algorithm (Hall, Riggs, and Salomonson*.,* 1995; Hall et al., 1998) uses a grouped thresholding technique, and will produce daily and 10-day composite lake ice products.

Given the regional nature of lake ice conditions, the MODIS algorithm will require extensive validation activity, pre-launch and in-flight, to build up regional databases of factors influencing ice conditions. It is expected that the VIIRS algorithm will benefit from these databases.

2.2.2.2   MODIS Airborne Simulator

MODIS pre-launch activity uses data from the various campaigns of the MODIS Airborne Simulator (MAS). We will also make use of this data for initialization and pre-launch characterization, as we discuss in Section 3.5.6 of this document. MAS data have also been used for our EDR performance analysis (c.f. Section 3.3.4.2).

2.2.2.3 Passive Microwave

Passive microwave observations of first year sea ice have made a valuable contribution to the study of polar regions (Eppler *et al.,* 1992). Studies of lake ice have been much less extensive, perhaps because of limited availability of high spatial resolution microwave data. The few studies that have been made include airborne C-band radiometry of the Great Lakes (Swift, Jones *et al.,* 1980; Swift, Harrington *et al.,* 1980) and airborne Ka-band imagery of Lake Harding, Alaska (Melloh *et al.,* 1981). These studies demonstrate the potential for passive microwave remote sensing of lake ice. They show that lake ice types can be distinguished by their microwave brightness temperatures.

A uniform slab of clear ice will emit microwave radiation proportional to its thickness. In lake ice, there can be many air bubbles which are unevenly distributed throughout the ice. The bubbles lower the emissivity, resulting in brightness temperature variations (Hall *et al.,* 1981). Surface features, produced by freeze/thaw events and motion-driven collisions, will also modify the microwave signal (Eppler et al., 1992). The same features affect surface albedo, suggesting correlations between microwave and reflectance signatures of lake ice.

Lake ice cover is a requirement for the NPOESS/CMIS passive microwave sensor, at a horizontal spatial resolution of 20 km. The potential exists for a beneficial fusion of VIIRS and CMIS data.

2.3 INSTRUMENT CHARACTERISTICS

The VIIRS sensor is being designed based on the NPOESS sensor requirements and EDR thresholds and objectives. The Fresh Water Ice algorithm uses surface reflectance for daytime retrievals, and surface temperature for nighttime retrievals. Following the suggestion of the VIIRS SRD, and based on our own analysis, we will use the VIIRS bands at the imagery (fine) resolution. The performance characteristics of the VIIRS bands are obtained from the Raytheon VIIRS Sensor Specification Document *[PS 154640-101]* and the VIIRS RDR to SDR Conversion ATBD *[Y3261]*.

Tables 2 and 3 list the characteristics of the bands used by the Fresh Water Ice algorithm.

Table 2. Fresh Water Ice EDR – Input Data Summary (Spatial)

$\lambda(\mu m)$	m)	GSD (m) at Nadir (Track x Scan)	HSR (m) at Nadir (Track x Scan)	GSD (m) at Edge of Scan (Track x Scan)	HSR (m) at Edge of Scan (Track x Scan)
0.645	0.050	371 x 131	371 x 393	800 x 800	800 x 800
0.865	0.039	371 x 131	371 x 393	800 x 800	800 x 800
11.45	1.9	371 x 131	371 x 393	800 x 800	800 x 800

Table 3. Fresh Water Ice EDR – Input Data Summary (Radiometric)

$\lambda(\mu m)$	m)	Ltyp (W/m2-sr-um) or Ttyp	SNR / NEdT at Nadir	SNR / NEdT at Edge of Scan
0.645	0.050	22.0	317.9	183.5

0.865	0.039	25.0	418.7	241.7
11.45	1.9	210 K	0.43 K	0.74 K

2.4   RETRIEVAL STRATEGY

Automated algorithms will be used to derive ice edge location and ice concentration. The algorithms will function in the Snow/Ice Module, as an integral part of the software architecture for producing Snow/Ice EDRs as well as Imagery ARPs. The processing outline is described in Section 3.1.

Although ice edge location and ice concentration are application-related products of the Imagery EDR, similar algorithms and input data are used for the Fresh Water Ice Sea Ice Age/Edge Motion EDRs. There is a large degree of commonality between the algorithm theoretical basis for Imagery Sea Ice ARPs *[Y2466]* and that for Fresh Water Ice.

The derivation of the VIIRS Fresh Water Ice EDR requires a series of preprocessing steps.

The input data will consist of a two-dimensional grid of surface pixel data (image) for each VIIRS band. It is expected that the images will be in the form of surface reflectance and surface temperature.

The algorithm will acquire surface reflectance in Visible and Near-Infrared bands from the VIIRS Surface Reflectance Intermediate Product (IP), which is produced by the Atmospheric Correction Over Land algorithm *[Y2411]*.

The algorithm will acquire a VIIRS Surface Temperature IP from the Ice Surface Temperature algorithm *[Y2405]*.

The algorithm will acquire a cloud mask from the VIIRS Cloud Mask IP *[Y2412]* to identify pixels that should be excluded from processing due to cloud or cloud shadow. The Cloud Mask IP will also include a land/water mask.

The algorithm will acquire a VIIRS Fresh Water Mask IP to identify all pixels which should be processed for the Fresh Water Ice EDR. This mask defines the Horizontal Coverage specification of the EDR. It excludes all fresh water bodies smaller than 10 km in any direction.

3.0   ALGORITHM DESCRIPTION

3.1   PROCESSING OUTLINE

The algorithm of ice concentration and ice edge boundary retrieval have changed since the version 2 ATBD, due to new requirements. Instead of using spectral mixture analysis to select ice tie points, we now select tie points from the local distribution of surface temperature and/or surface reflectance. Surface temperature and surface reflectances are derived from TOA radiances in the fine resolution (imagery) bands.

The process flow for the automated production of the Fresh Water Ice EDR is described in the VIIRS Snow/Ice Module Software Architecture document *[Y2477]*. The main steps are as follows:

1) Input data, described in Section 3.2, is read in to the module. Pixels within the pre-specified horizontal coverage range are passed into the ice units, beginning with the ice concentration unit.

2) The surface reflectance image is passed into the ice concentration unit. Pixels with bad quality, land, cloud, and solar zenith angle flags are masked. Ice concentration is calculated for each good pixel.

3) The surface temperature image is passed into the ice concentration unit. Pixels with bad quality, cloud, and cloud flags are masked. Ice concentration is calculated for each good pixel.

4) The combined ice concentration for each pixel is calculated as the weighted mean of the individual band results. The band weights are derived from the RMS variation in that band.

5) The ice concentration is passed into the ice edge location unit. Pixels with no concentration result are masked. The ice edge location algorithm tags each pixel as edge or no edge, and computes edge location coordinates from the coordinates and concentration of each edge pixel and its neighbors.

The algorithm shares functionality with the new version 3 automated algorithm for the retrieval of Imagery Sea Ice Data products. Therefore, the theoretical basis and performance of the Fresh Water Ice EDR is quite similar to that for sea ice, as documented in the VIIRS Imagery ATBD *[Y2466]*.

The algorithm uses reflectance and surface temperature data obtained from intermediate products (IPs) produced from the Daytime Visible (DV) and Long-Wave Infrared (LWIR) imagery bands to meet the threshold requirements. Performance may be enhanced by the use of the Near Infrared (NIR) fine resolution band at 0.865 μm. The relative weight assigned to the DV and NIR bands shall be determined by initialization and validation (c.f. Section 3.6). Data shall be masked using a land/water mask prepared from NASA GTOPO30 or other applicable topographic or geographic data sets providing compatible spatial resolution. Following

application of the land/water mask, data shall be masked using a cloud mask. The Cloud Mask IP *[Y2412]* is generated at the VIIRS moderate resolution. A fine resolution cloud mask, also available as part of the Cloud Mask IP, may improve performance.

3.2   ALGORITHM INPUT

3.2.1   VIIRS Data

For optimal performance of the algorithm, the VIIRS data presented in Table 4 are required.

Table 4. Ancillary VIIRS data for the Fresh Water Ice EDR

Input Data	Source of Data	Reference
Instrument SDR Quality	VIIRS RDR to SDR Conversion	*[Y3261]*
Geo-location	VIIRS Earth Location Algorithm	*[Y3258]*
Solar/Sensor Geometry	VIIRS RDR to SDR Conversion	*[Y3261]*
Visible Surface Reflectance	VIIRS Atmospheric Correction over Land Algorithm	*[Y2411]*
Near IR Surface Reflectance	VIIRS Atmospheric Correction over Land Algorithm	*[Y2411]*
Surface Temperature	VIIRS Ice Surface Temperature Algorithm	*[Y2405]*
Cloud Mask	VIIRS Cloud Mask Algorithm	*[Y2412]*
Fresh Water Mask	VIIRS RDR to SDR Conversion	*[Y3261]*

3.2.1.1   Instrument Quality

Each cell of the image cube will have its own quality flag. Cells with quality below a threshold, to be determined, shall be excluded from further processing.

3.2.1.2   Geo-location

Geo-location of each imaged pixel will be used to report the latitude/longitude coordinate of each horizontal cell of the ice concentration product, and to report the ice edge location coordinates.

3.2.1.3   Solar / Sensor Geometry

The solar zenith angle will be used to determine the relative weight of the reflectance-based and temperature-based retrievals. Reflectance data will be progressively de-weighted as the solar zenith angle increases, providing a seamless transition across the terminator. The weighting function will be determined by pre-launch validation, as part of the initialization plan, and will be adjusted by post-launch validation. Solar/sensor geometry will be used to apply a BRDF quality flag, if warranted by pre-launch or post-launch validation.

3.2.1.4 Surface Reflectance

Discrimination of ice from open water can be made on the basis of their reflectance spectra. The VIIRS Atmospheric Correction Over Land algorithm [*Y2411*] will supply a surface reflectance intermediate product (IP) for the visible and near IR bands used by the algorithms. Models of surface reflectance error are used in our performance analysis (c.f. Section 3.4).

3.2.1.5 Surface Temperature

Surface temperature of the ice is needed for ice concentration retrieval at night, and is often useful for daytime retrievals. The VIIRS Ice Surface Temperature algorithm *[Y2405]* will determine the temperature of ice surfaces for each imaged pixel, which will be supplied as a Surface Temperature Intermediate Product (IP). A model of surface temperature error is used in our performance analysis (c.f. Section 3.4).

3.2.1.6 Cloud Mask

The VIIRS cloud mask *[Y2412]* is expected to derive a status of clear/probably clear/probably cloudy/cloudy for each pixel, following the convention of the MODIS cloud mask (Ackerman *et al.*, 1997). Pixels flagged as "cloudy" will be excluded from further processing. We expect that pixels flagged as "probably cloudy" will also be excluded. This determination must depend on an assessment of the cloud mask performance, particularly over snow and ice surfaces. Pixels flagged as "probably clear" will be processed, although we wish to flag the output EDR as "possibly cloud contaminated." Pixels flagged as "definitely clear" will be processed. It is anticipated that the cloud mask will also flag pixels that are shadowed by clouds. In that case, a cloud shadow quality flag will be assigned to those pixels. Ice edges are often associated with cloud edges, increasing the critical need for effective cloud masking.

3.2.1.7 Fresh Water Mask

The Horizontal Coverage for the EDR is specified as a global set of fresh water bodies which have a minimum spatial extent of 10 km in any direction. This set will be pre-selected and mapped to a global grid. VIIRS pixels co-located with this set will be tagged as fresh water. Only pixels with this fresh water mask will be processed by the algorithm. The fresh water mask will be supplied by the Build-SDR module *[Y3261]*.

3.2.2 Non-VIIRS Data

The Fresh Water Ice EDR requires no input data from outside the VIIRS system.

3.3 THEORETICAL DESCRIPTION OF THE RETRIEVAL

In the following sections, the mathematical background of the processes outlined in Section 3.1 will be described. These processes only apply to regions that successfully passed the quality examinations.

3.3.1 Physics of the Problem

3.3.1.1 Ice Reflectance

Reflectance from ice surfaces differs from snow reflectance because the ice consists of sheets rather than grains. Clear ice slabs are highly transmitting (Bolsenga, 1983). Reflectance occurs by scattering from impurities, such as brine pockets and air bubbles. Therefore, the reflectance observed from natural ice surfaces is highly variable, depending on the condition of impurities for a given ice sheet. Given the wide variety of ice conditions in nature, ice reflectance is not as well determined as snow reflectance. Snow reflectance is amenable to the Mie scattering theory (Warren, 1982). In contrast, studies of ice reflectance tend to be empirical.

Jeffries, Morris, and Weeks (1994) studied shallow lakes on the North Slope of Alaska. They noted that lake ice is comprised primarily of congelation ice. That ice is the product of downward growth of ice crystals into the water, as heat is conducted through the ice, from the growth interface to the atmosphere. This ice can be either clear, or contain bubbles. During the earliest stages of ice growth, all gases are rejected back into the water during the freezing. This results in a layer of clear, low reflectance ice. The ice layer thickens downward, with the new layers, shielded from the atmosphere, retaining air bubbles (Morris, Jeffries, and Weeks, 1995). This growth process differs from sea ice growth, which initiates with the formation of frazil ice in turbulent, briny media (Eppler *et al.,* 1992). As a result, young sea ice reflectance spectra may differ from lake ice spectra.

The reflectance properties of fresh water ice have been studied by Leshkevich (1981), who identified seven distinct types of ice cover on Green Bay from a supervised classification of Landsat data. Differences between this classification and a previous automated classification of the same scene (Leshkevich, 1985) point to the need for a more comprehensive, well-documented library of ice type signatures. The differences also demonstrate the difficulty in classifying ice types, which are inherently variable.

One drawback to the classification of fresh water ice types has been the relative scarcity of remote sensing studies of lake ice. Remote sensing studies of young sea ice are more widespread, and are of potential benefit (Eppler *et al.,* 1992). One well-established characteristic of sea ice is the wide range in albedos observed in first-year ice of various types and thickness (Grenfell and Maykutt, 1977; Grenfell and Perovich, 1984). This characteristic appears to be shared by fresh water ice (Bolsenga, 1983). This characteristic is an important limiting factor in reflectance-based retrieval of ice concentration in the absence of snow cover (Massom and Comiso, 1994).

3.3.1.2 Snow reflectance

The reflectance characteristics of ice surfaces are influenced by accumulated snow cover.

Pure snow is a distinctive target across a part of the solar spectrum. It is among the brightest of natural substances in the visible and near-infrared part of the spectrum, but it is also often the darkest in the shortwave infrared (Dozier, 1989). The spectral albedo of snow depends on wavelength, and this dependency is controlled by the imaginary part *(k)* of the complex refractive index. This reaches a minimum at a wavelength of about 0.46 microns, and increases by a factor of 10^6 - 10^7 as wavelength increases out to 2.5 microns (Warren, 1982; Dozier, 1989).

Light transmission decays exponentially in snow across a distance *d* as exp(-4πkd/λ). The *e-*folding distance for snow (the distance over which transmittance is reduced to 1/e) decreases from more than 20 m in the 0.4 – 0.5 micron range to less than 1 mm at 1.6 microns.

Light in snow is scattered primarily by refraction through, not reflection from, the ice grains. Photons are scattered at the grain surfaces, but absorbed while traversing the grain interiors. Only about 3 percent of the light scattered by an ice grain is reflected from the external surface. Nearly 89 percent is refracted through the grain, and 8 percent is scattered after internal reflections (Bohren and Barkstrom, 1974). Because ice is so transparent to visible radiation, snow reflectance is insensitive to grain size in bands below 0.7 microns, but sensitive to absorbing impurities in the snow and to SWE (Wiscombe and Warren, 1980; Grenfell, Perovich, and Ogrin, 1981). Because absorption by ice is much stronger in bands above 1.4 microns, reflectance at these wavelengths is insensitive to absorbing impurities and SWE, but sensitive to grain size. Absorbing particulates affect snow reflectance out to 0.9 microns (Grenfell, Perovich, and Ogrin, 1981), so the 0.86 micron band is sensitive to both absorbing impurities and grain size. All aforementioned values in this paragraph are determined from geometric optics for a sphere.

The spectral signature of snow is unique among common substances. Clouds and snow are both bright across the visible and near-infrared region, but clouds are much brighter than snow in the shortwave infrared. This is because the smaller size of the scatterers in clouds decreases the probability of absorption in this spectral region where ice and water are moderately absorptive (Crane and Anderson, 1984; Dozier, 1984, 1989). Conversely, bodies of open water are dark at all wavelengths.

The physical basis of snow reflectance is also discussed in the VIIRS Snow Cover/Depth ATBD *[Y2401]*.

3.3.1.3 Surface temperature

During nighttime, infrared bands will be the only available information to retrieve ice fraction. Infrared radiance allows us to calculate surface temperature.

Ice surface temperature is a good indicator of ice state for ice with thickness less than 1 meter. The surface temperature varies in a large range of magnitude depending on the stage of ice development or ice age (thickness). Thus, surface temperature is an indicator of ice age.

Changes in ice surface temperature are governed by the joint influence of vertical heat fluxes of different origin. The intensity of turbulent exchange by heat between the atmosphere and underlying ice surface, as well as the surface balance of long-wave radiation, directly depend on ice surface temperature. Vertical heat flux through ice cover is an explicit function of the vertical ice temperature profile, which depends on ice surface temperature. Thus, all main components of heat exchange between the atmosphere and the underlying ice surface (except short-wave radiation fluxes) are explicit functions of ice surface temperature.

In wintertime, heat flux between the atmosphere and ice is compensated by ice growth at the underside of the ice. There are no vertical changes in heat flux at the boundary between air and ice surface. At the same time, many components of heat flux depend on ice surface temperature.

Therefore, conditions of conservation of vertical heat flux at the surface can be fulfilled only if ice surface temperature is adjusted to varying influencing environmental conditions.

Ice thickness is the main factor determining vertical heat flux through the ice under specified atmospheric conditions. Thus, a general conclusion about the relation between ice surface temperature and thermodynamic processes in ice cover and atmospheric boundary layer can be formulated. Ice surface temperature is determined by the processes of vertical heat exchange and is a distinctive indicator of ice thickness.

3.3.1.4 Physical Hypotheses

A. Both surface temperature and reflectance measured on the basis of satellite data vary in a large range of magnitude depending on ice fraction and ice age. Thus, surface temperature and reflectance are a valuable source of information on ice fraction and age in the cell as the surface temperature and reflectance of a mixed ice/water pixel will depend on ice fraction as well as ice type. To separate the influence of ice fraction and ice type, we need to use an additional assumption about these two influencing parameters.

Our approach is based on a consideration of processes forming ice distribution. Spatial changes in the predominant ice type (age) and its properties are governed by freezing and melting and can be considered as smooth. This hypothesis, which is certainly correct in most cases, is used to develop the algorithm of ice concentration retrieval.

B. Fresh water ice consists of different floating ice forms (ice floe sizes). The sizes of ice floes depend upon season and region decreasing during melting. A predominant ice floe size also decreases with decrease in ice concentration. But even ice floes of small size tend to gather in belts or spots of very close ice. As a result, we can state that in almost all cases, data of satellite observations even for relatively small areas of the surface will include pure pixels corresponding to ice.

Our approach takes advantage of the overwhelming probability that an ice scene will contain pure ice pixels in a region localized near any pixel that contains some ice. In that case, the condition of the predominant ice type in the area under consideration can be approximated as the reflectance (or temperature) peak of the distribution (histogram) of reflectance (or temperature). Our approach adopts the derived condition of the predominant ice type as the ice tie point for a given pixel.

C. Tie point analysis determines the fraction of ice. The tie point analysis is based on the assumption that the spectral fraction of ice is equal to the horizontal fraction of the pixel covered by ice. The ice tie point is reflectance (or temperature) of ice in various stages of development. These ice tie points are not predetermined but vary in large range depending on time and space. The tie points are scene specific and calculated by an automated algorithm, promising global operational capability.

D. Ice concentration is derived independently from three bands (visible reflectance from the 0.645 μm imagery band, near IR reflectance form the 0.865 μm imagery band, and temperature from the 11.45 μm imagery band). We use the reflectance tie points if the solar zenith angle is smaller than a threshold value. We use the temperature tie point if it is colder

than a threshold value. If all tie points are useful, we calculate a weighted average ice fraction. The relative weights of the three bands are determined automatically from the conditions of a specific scene. Optimized band weights reduce error and provide a seamless day/night transition.

3.3.2   Mathematical Description of the Fresh Water Ice Algorithm

3.3.2.1   Ice Concentration from Tie Points

Under conditions where there is a predominant ice type in a local area, ice fraction for each imaged pixel can be retrieved by the direct application of a tie point method. The tie point is a special case of spectral mixture analysis, restricted to two endmembers. The endmember signatures are derived from identifying pure pixels in the scene.

The ice fraction for a mixed pixel is:

$$f(p) = (b_p - b_{water}) / (b_{ice} - b_{water}) \tag{3.3-1}$$

where: *$f(p)$ is the calculated ice fraction*
                      b_{ice} is the brightness value of a pure ice pixel
                      b_{water} is the brightness value of a pure water pixel
                      b_p is the brightness value of the pixel

Our algorithm acquires three independent brightness values for each pixel. These are a visible reflectance, a near IR reflectance, and a temperature.

To take advantage of all of the available information, our algorithm generalizes the tie-point equation to three dimensions. We assume that the locus of equal ice fraction in multi-dimensional space corresponds to planes perpendicular to the line connecting ice and water tie points. In that case:

$$f(p) = \Sigma_j (b_{jice} - b_{jwater})(b_{jp} - b_{jwater}) \ / \ \Sigma_j (b_{jice} - b_{jwater})^2 \tag{3.3-2}$$

      where: *$f(p)$ is the calculated ice fraction*
                            b_{jice} is the jth brightness value of a pure ice pixel
                            b_{jwater} is the jth brightness value of a pure water pixel
                            b_{jp} is the jth brightness value of the pixel

and the brightness values in Equation 3.3-2 have been normalized to their root mean square deviations on the scene. In that case, equation 3.3-2 is equivalent to:

$$f(p) = (\Sigma_j (w_j)(b_{jp} - b_{jwater}) / (b_{jice} - b_{jwater})) / \Sigma_j w_j \tag{3.3-3}$$

      or:

$$f(p) = \Sigma_j (w_j \ f_j(p)) / \Sigma_j w_j \tag{3.3-4}$$
      where: *$f(p)$ is the calculated ice fraction*

w_j is the relative weight in band j
b_{jice} is the jth brightness value of a pure ice pixel
b_{jwater} is the jth brightness value of a pure water pixel
b_{jp} is the jth brightness value of the pixel
$f_j(p)$ is the ice fraction calculated from band j

and: $\quad w_j = E_j (b_{jice} - b_{jwater})^2$ $\hspace{4cm}$ (3.3-5)

We see that the relative weights of the bands scale as the square of the difference in ice and water tie points relative to the RMS deviation of the scene. The factor E_j is included to allow for other band-dependent factors, such as solar zenith angle. To some extent, the degrading effects of large solar zenith angle will be found in increased RMS deviation in the reflectance bands. It must be determined whether an extra E_j factor is needed. This will be a goal of initialization.

Our approach is to calculate ice fraction for each band, according to equation 3.3-1, and derive a band-weighted ice fraction, according to equation 3.3-4, with band weights determined by equation 3.3-5.

Errors in deriving b_{ice} and b_{water} have been an obstacle to achieving global operational ice concentration retrieval. Our algorithm greatly reduces these errors by deriving tie points from the scene.

An ice/water threshold is derived to select the pixels used for the water distribution for scenes containing open water. We assume that a scene-corrected threshold corresponds to the minimum probability of reflectance and/or temperature located between values associated with water and ice. Location of the minimum is found by use of a sliding integral taken over the probability density of the parameter (reflectance or temperature). The range of measured parameter values is divided into a specified number of histogram bins. The histogram of the distribution for the scene is computed. The histogram is smoothed by a running boxcar filter of specified width, producing a sliding integral of the parameter distribution. The lowest value of the sliding integral is adopted as the ice/water threshold.

The water tie point is selected as the maximum in probability density distribution corresponding to the maximum of the sliding integral over water reflectance (temperature). We analyze water characteristics only in the immediate vicinity of the ice zone. It allows us to improve the accuracy of water tie point determination as it eliminates water characteristics for areas far away from ice cover. Those characteristics can differ from open water properties in the vicinity of the ice zone.

A scene-corrected ice threshold is derived as the first minimum of the sliding integral of the parameter distribution. The water tie point is selected as the maximum of the sliding integral below the ice/water threshold.

Figure 1 illustrates the process.
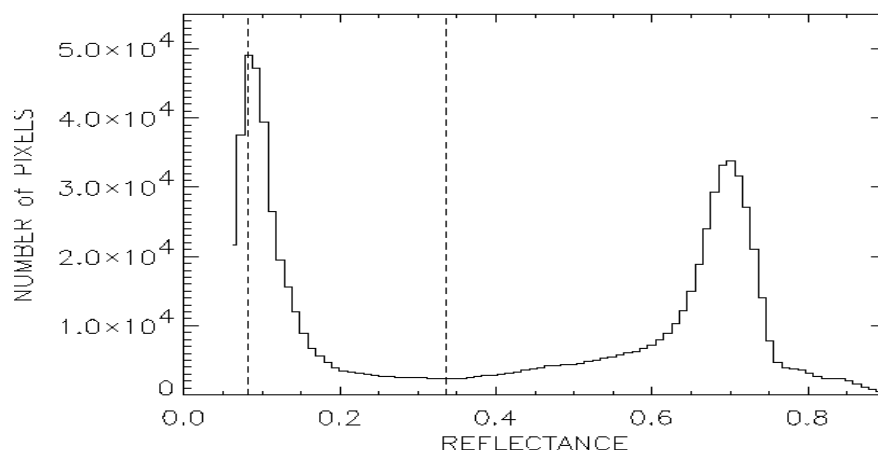
Figure 1. Distribution of 645 nm reflectance for an ice/water scene. The ice/water threshold reflectance (0.336) and the water tie point (0.083) are indicated.

For every imaged pixel, ice reflectance and/or surface temperature corresponding to an ice tie point (pure pixel) is calculated as the most probable reflectance and/or ice surface temperature in the vicinity of the pixel under consideration.

The ice tie point is derived locally for each pixel whose parameter value is on the ice side of the ice/water threshold. The distribution of parameter values in a local search window is acquired. The ice tie point is selected as the maximum value for a sliding integral of the local parameter distribution. Figure 2 illustrates the process.
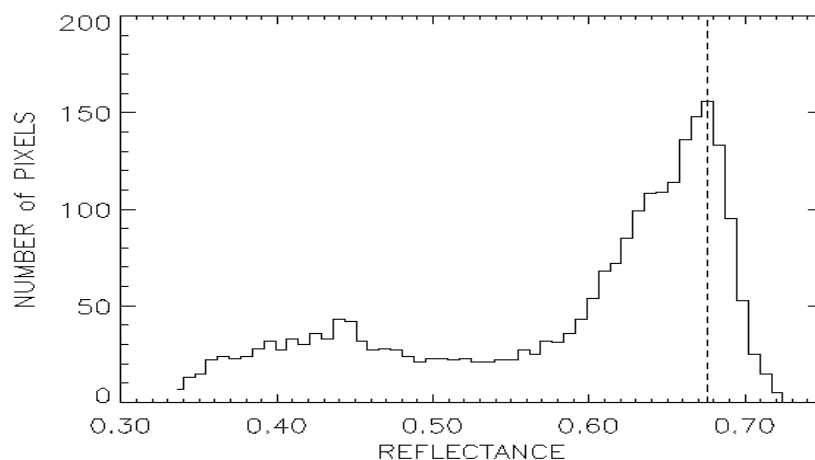
Figure 2. Distribution of 645 nm reflectance for a local search window centered on a single pixel of the scene.

For each pixel, a search window is used to establish the ice tie points from the local distribution of reflectance and/or surface temperature at the spatial scale of the window. The ice tie point is selected as the maximum value for a sliding integral of the local parameter distribution within

the search window. For the example presented in Figure 2, the ice tie point for the pixel is equal to 0.676. The accuracy of the ice tie point selection depends on the size of the local search window. Optimization of the search window size will improve algorithm performance.

Having selected the ice and water tie points appropriate to a given pixel, the algorithm applies equation 3.3-1 to retrieve the ice fraction for each pixel. Ice concentration is reported as the ice fraction of each pixel. Concentrations less than 0.0 are set to 0.0. Concentrations greater than 1.0 are set to 1.0.

3.3.2.2   Ice Edge Boundary

Gridded ice fraction at imagery resolution is used to calculate ice edge boundary. A pixel is tagged as a possible ice edge pixel if one of the following conditions are met:

(1) It has ice concentration greater than 0.1 and at least one neighboring pixel has ice concentration less than 0.1

(2) It has ice concentration less than 0.1 and at least one neighboring pixel has ice concentration greater than 0.1

The set of tagged pixels are examined to derive ice edge isolines and ice edge coordinates. Each neighboring pair of tagged pixels will produce an edge coordinate and an edge pixel. The edge pixel will be that member of the pair whose concentration is closer to the 0.1 edge value. The edge latitude/longitude coordinate is derived by a weighted linear interpolation of the pixel coordinates:

$$\text{Lat} = (\text{Lat})_2 + (((\text{Lat})_1 - (\text{Lat})_2) \times (0.1 - C_2) / (C_1 - C_2)) \tag{3.3-6}$$

$$\text{Lon} = (\text{Lon})_2 + (((\text{Lon})_1 - (\text{Lon})_2) \times (0.1 - C_2) / (C_1 - C_2)) \tag{3.3-7}$$

where : $C_{1,2}$ are the ice concentrations for pixels 1 and 2

and the coordinates apply to the pixel centers, as supplied by the geo-location algorithm *[Y3258]*.

Our algorithm also provides the option to retrieve the boundary of a diffusive ice edge by smoothing the ice concentration on an appropriate spatial scale. Different applications require different spatial scales of smoothing. Our algorithm allows for a flexible choice of smoothing kernel defined by specialized users' needs.

3.3.3   Archived Algorithm Output

Ice concentration will be archived as gridded products corresponding to imagery pixels.

Ice edge boundary will be archived as a contour on a map (an ice edge isoline) and as a set of latitude/longitude coordinates. The resolution will depend on the spatial scale at which the ice concentration is smoothed. It will range from imagery resolution, for unsmoothed concentration appropriate to a compact edge, to coarser resolution characteristic of diffusive ice edges.

Data quality flags will be attached to any reported product derived from input data with a data quality flag attached. These include, but are not necessarily limited to, data flagged as "probably clear", "cloud shadow", and "coastline".

3.4 PERFORMANCE

The performance of the algorithms with respect to the VIIRS requirements and the System Specification (c.f. Table 1) is reviewed in this section.

3.4.1 Stratification

During Phase I of the NPOESS project, performance shall be verified by analysis, modeling, and/or simulation based on the instrument design and performance characteristics and the algorithms. The analysis, modeling, and/or simulation shall be sufficiently extensive in scope to verify that EDR requirements are met under a broad range of conditions that are representative of those occurring in nature, including both typical and extreme conditions.

3.4.1.1 Ice Concentration

We identify the following stratifications for ice concentration:

1) Ice concentration "truth"

2) Ice "type"

3) Day/Night

4) Viewing angle

Performance of the ice concentration algorithm is expected to depend on ice concentration "truth". A sensible stratification must then include ice concentration "truth" as a parameter. We have selected 4 ranges of ice concentration, 0.0-0.35, 0.35-0.65, 0.65-0.85, and 0.85-1.0. These ranges correspond to the following ice concentration zones: very open floating ice, open floating ice, close floating ice, very close floating ice.

Ice conditions are widely variable, depending on its stage of development. The contrast between ice and water tie points is generally larger for ice in later stages of development. Algorithm performance is very sensitive to tie point contrast. Analytically, the error in concentration derived from a tie point equation scales inversely with the tie point contrast. A sensible stratification should include ice "type" as a parameter. We have selected 2 ice types, "Young", and "First-Year or Older". Young ice is characterized by a thickness of 0.1 – 0.3 meters. We select 0.3 meters as our boundary between ice types. Our specification for ice concentration measurement uncertainty (c.f. Table 1) excludes ice with characteristic thickness less than 0.1 meter ("New Ice" and "Nilas").

We include a third stratification by type, which we call "Typical Scene", to illustrate expected performance for a typical probability of ice types.

We specify performance at nadir and at edge of scan.

Nighttime and daytime retrievals are distinct. Daytime retrievals can use reflectance data as well as temperature data. Because thermal contrast between ice and water is smaller during the daytime, a daytime retrieval will rely more heavily on reflectance data. Nighttime retrievals, on the other hand, must rely solely on temperature data.

We have used a solar zenith angle of 60 degrees in our simulations to date. Our stratification of solar zenith angle is restricted to this value. A wider range of solar zenith angles shall be simulated in the future, following the development of surface reflectance error simulations over a wider range.

We report performance estimates for a representative sample of geophysical conditions:

Case 1: Clear, Nadir, Solar Zenith Angle = 60 degrees

Case 2: Clear, Nadir, Night, Air Temperature = -5 degrees Celsius

Case 3: Clear, Nadir, Night, Air Temperature = -10 degrees Celsius

Daytime performance will depend on solar zenith angle, as surface reflectance errors increase with decreasing sunlight and increased atmospheric path length. We have modeled surface reflectance error for a solar zenith angle of 60 degrees to represent a typical solar elevation in sub-arctic regions during summertime.

Nighttime performance will depend on the surface air temperature. The thermal contrast between ice and open water increases as air temperature decreases. For an air temperature of 0 Celsius, the thermal contrast between most first year ice types and water is negligible. For an air temperature of –5 Celsius, the thermal contrast between most first year ice types and water is 3 – 4 degrees. For air temperatures colder than –10 Celsius, the thermal contrast between most first year ice types and water is greater than 8 – 10 degrees. We have selected two cases of nighttime air temperature (-5 Celsius and –10 Celsius) to illustrate the relative effect on performance. We have found that performance at colder temperatures is similar to the performance at –10 Celsius.

3.4.1.2 Ice Edge Boundary

Ice edge boundary is derived directly from ice concentration. For this reason, its stratification is similar to that of ice concentration. We identify the following stratifications for ice edge boundary:

1)   Ice "type"
2)   Sensor view angle
3)   Day/Night

Note that the ice concentration "truth" is not included as a stratification, because by definition the retrieval occurs at ice edges only.

The rationales for our stratifications are identical to the ice concentration stratification rationales discussed in Section 3.4.1.1, with the exception of ice concentration "truth".

3.4.2 Stratified Performance Analysis

3.4.2.1 Ice Concentration

Ice Concentration is derived by a tie point equation:

$$C = (P-W) / (I-W) \tag{3.4-1}$$

Where: P = measured parameter (either surface temperature or surface reflectance)
     W = water parameter value (tie point)
     I = ice parameter value (tie point)

Errors in P, W, and I contribute to the measurement uncertainty:

$$\sigma^2_C = (\sigma^2_P + C^2 \sigma^2_I + (1-C)^2 \sigma^2_w) / (I-W)^2 \tag{3.4-2}$$

Errors in P are derived from sensor and algorithm, and are taken from the stratified performances of the Surface Reflectance and Surface Temperature Intermediate Products (IPs). These are documented in the VIIRS System Specification *[SS 154640-001]* and in the VIIRS Imagery TIM *[Y4963]*. Precision and accuracy errors were applied to our test data sets.

I and W are derived from a scene, using search windows. Errors in I and W, caused by deviations of the derived ice and water tie points from the "true" pixel tie points, have been an obstacle to achieving global operational ice concentration retrieval. Our algorithm greatly reduces these errors by deriving tie points from the scene.

Our analysis of ice concentration measurement uncertainty was performed as follows:

We applied our algorithm to MODIS Airborne Simulator (MAS) scenes at a 50 meter pixel resolution. The test scenes are discussed in the VIIRS Test Data Set Specification Document. Reflectances in MAS band 3 (648 nm) and 7 (866 nm) were calculated from the TOA radiances. Brightness temperatures in MAS bands 45 (11 μm) and 46 (12 μm) were calculated from the TOA radiances. Surface temperature was computed by the Surface Temperature IP algorithm. The surface reflectances and surface temperature at 50 meter resolution were used as input data for our algorithm. The retrieved ice concentration was adopted as "truth". The 50 meter truth was aggregated to a VIIRS pixel size at nadir (8 x 8 aggregation to 0.4 km pixels) and adopted as VIIRS "true" concentration at nadir. An additional 16 x 16 aggregation was made to obtain VIIRS "true" concentration at 0.8 km (edge of scan).

A model MTF with HSR = 0.4 km was then applied to the surface reflectance and surface temperature images to simulate VIIRS imagery at nadir. An additional MTF with HSR = 0.8 km was applied to simulate the edge of scan imagery.

We then perturbed the MTF-smeared reflectances, using our model errors for the Surface Reflectance IP in VIIRS band I2 (645 nm), which is the daytime visible (DV) imagery band. The errors depend on surface reflectance truth, which is correlated with ice concentration. Accuracy and precision errors were applied. Accuracy errors include a 2% calibration bias and an aerosol optical thickness bias of 0.05. Precision errors are derived from the sensor noise. Reflectance

errors were calculated for a solar zenith angle of 60 degrees. We note that VIIRS band I3 (865 nm) is also available as a performance enhancement band. The daytime performance reported here is from the 645 nm VIIRS band only.

We perturbed the aggregated temperatures, using model errors for the Surface Temperature IP. Surface Temperature IP performance was derived as follows:

The split-window Ice Surface Temperature algorithm was applied to MODIS Airborne Simulator (MAS) scenes at a 50 meter pixel resolution. Brightness temperatures in MAS bands 45 (11 mm) and 46 (12 mm) were calculated from the unperturbed TOA radiances in those bands, and used as input data to the algorithm. The retrieved surface temperatures were adopted as "truth". The 50 meter truth was aggregated to VIIRS imagery pixel sizes at nadir (8 x 8 aggregation to 0.4 km pixels). The aggregated temperatures were adopted as VIIRS "truth".

The MAS TOA radiances were then aggregated to VIIRS pixel size. A proxy for the VIIRS Long-Wave Infrared (LWIR) imagery band radiance was made from the average of the band 45 and 46 radiances. The VIIRS model radiances were then perturbed by our models for sensor noise and calibration bias. A 0.5% calibration bias was applied to all radiances. Sensor noise models for VIIRS bands M15 (11 μm), M16 (12 μm), and LWIR (11.45 μm) were applied to the corresponding radiances. The perturbed radiances were converted to brightness temperature, and used as input data to the Surface Temperature IP algorithm.

SurfaceTemperature IP accuracy, precision, and uncertainty errors were calculated from comparison of the retrieved surface temperature to the "truth". At nadir, these errors are 0.278 K in accuracy and 0.378 K in precision. At edge of scan, the precision error is 0.508 K.

We applied the algorithm to the perturbed VIIRS scenes to retrieve ice concentration, and computed measurement uncertainty by comparing the retrieved concentration to the "VIIRS truth". The pixel deviations between retrieved and true concentration were aggregated 2 x 2 to a horizontal cell of 0.8 km to represent a VIIRS nadir retrieval. The aggregated deviations were sorted into the four truth stratification bins. For each bin, the RMS of the deviations was computed as the measurement uncertainty for that bin.

We applied the algorithm to the perturbed VIIRS scenes to retrieve ice concentration, and computed measurement uncertainty by comparing the retrieved concentration to the "VIIRS truth". We did this for three sea ice day time scenes:

> A Bering Sea scene in early April (AK_74_14) from the Alaska-April 95 campaign.

> Two Beaufort Sea scenes in late May (ACE_65_3 and ACE_65_8) from the FIRE-ACE campaign.

And for a lake ice daytime scene:

> A Lake Superior scene in February (WIN_46_16) from the WINCE campaign.

An example of the procedure is illustrated for scene ACE_65_3 in Figure 3.

(a)   (b)   (c)

(d)   (e)   (f)
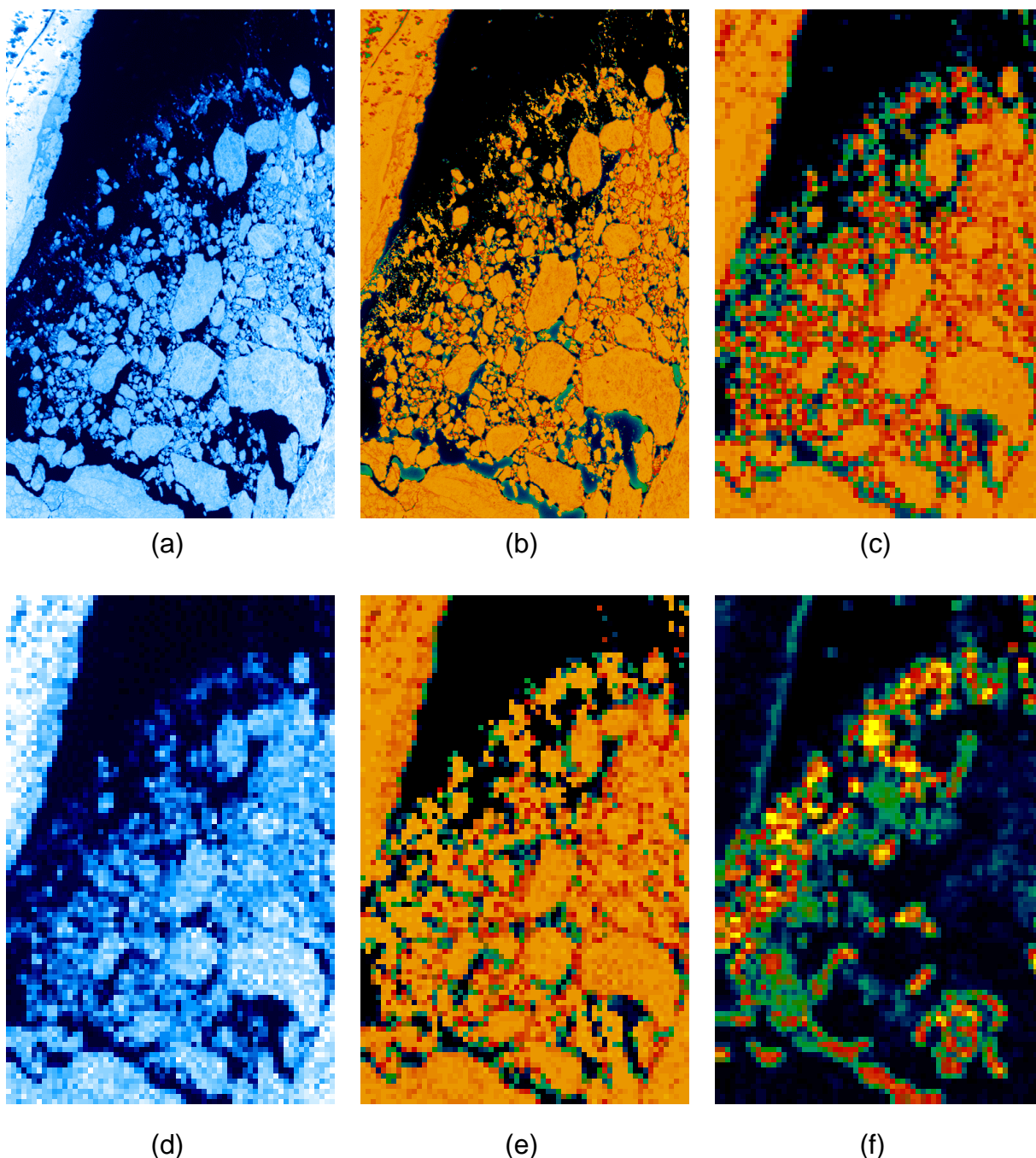
Figure 3. Illustration of the performance analysis methodology. The scene is from the FIRE-ACE campaign of the MODIS Airborne Simulator (ACE_65_3).

The original MAS scene (a), is used as input to the ice concentration algorithm, which derives ice concentration at the 50 meter MAS resolution (b). The concentration is aggregated to the VIIRS pixel size of 0.4 km to produce VIIRS truth (c). Scene (a) is then perturbed by our model for the sensor effects to simulate expected VIIRS imagery at nadir (d). Scene (d) is used as input

to the ice concentration algorithm, which derives the simulated VIIRS ice concentration (e). A comparison of result (e) with truth (c) produces an error estimate (f).

For daytime performance analysis, we use the reflectance data. For nighttime performance analysis, we use the surface temperature data, adjusted to simulate conditions when air temperature is –5 Celsius and –10 Celsius. The adjustment is necessary, because the nighttime thermal contrast between ice and water scales linearly with the thermal contrast between air and water:

$$T_W - T_I = 16.2\ H\ (\ 3.61 + 0.049\ T_W + (T_W - T_A\ ))\ /\ (1.5 + 17\ H) \tag{3.4-3}$$

Where: T_W = Water Temperature (Celsius)

T_I = Ice Temperature (Celsius)

T_A = Air Temperature (Celsius)

H = Ice Thickness (meters)

Equation 3.4-3 is derived from energy balance, and is approximately correct for ice thickness less than 1 meter and for typical nighttime conditions.

An illustration of the process is shown as Figure 4. The MAS scene AK74_14 was processed to create simulated nighttime surface temperature imagery for conditions where surface air temperature = 0^0 Celsius, -5^0 Celsius, -10^0 Celsius, and -20^0 Celsius.

(a) **(b)** **(c)**
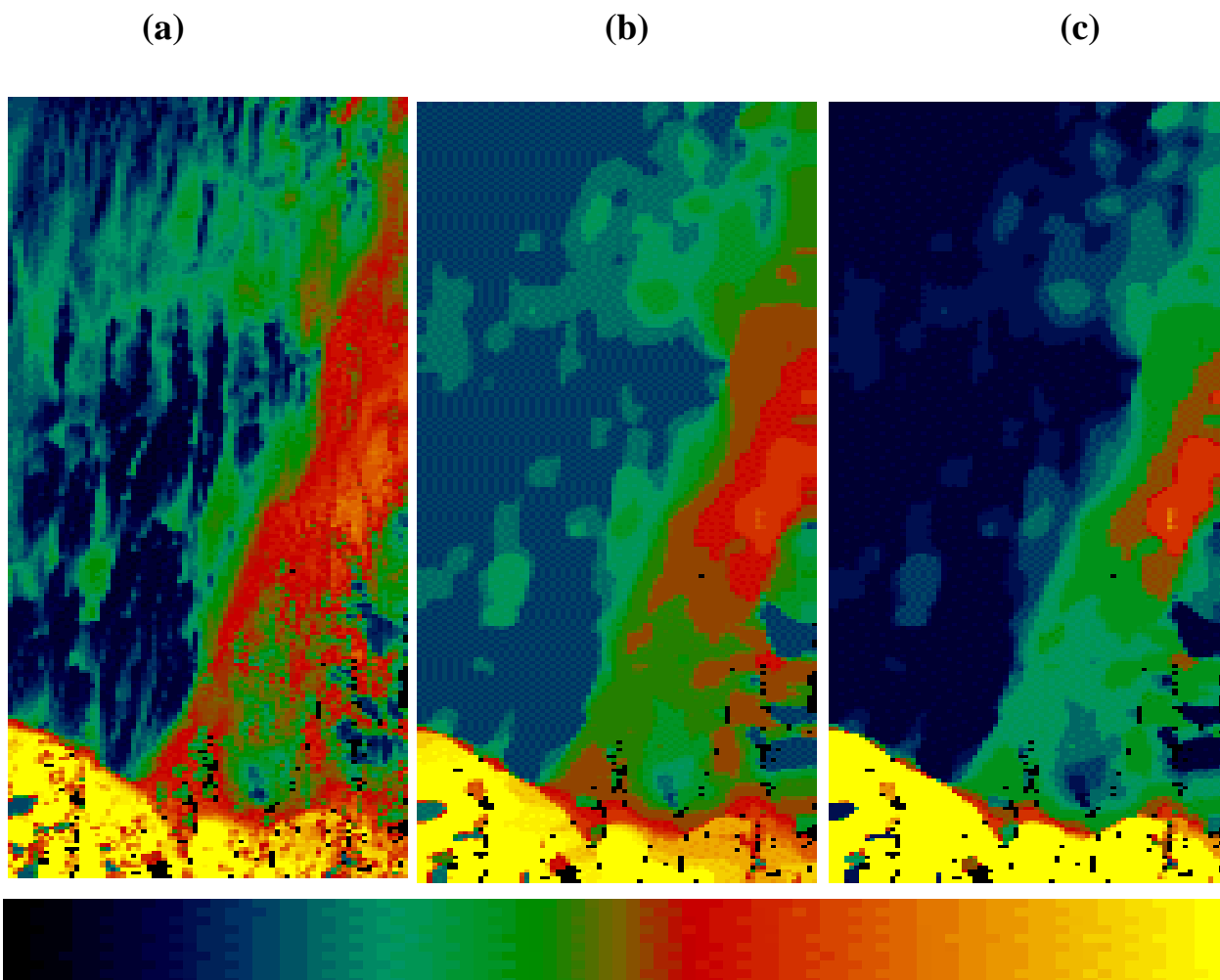
Figure 4. (a) Simulated VIIRS daytime visible band imagery of the Bering Sea scene AK74_14. (b) Retrieved ice reflectance tie points. (c) Ice thickness, derived from the reflectance tie points.

The color table displays a reflectance range of 0.0 (blue) to 0.7 (yellow) and a thickness range of 0.0 (blue) to 0.2 meters (yellow). The ice thickness, shown in Figure 4c, is calculated from a fourth order polynomial thickness-reflectance relation, which was determined empirically by matching temperature and reflectance distributions from a number of ice scenes.

The ice temperature was then calculated from equation 3.4-3, for a given air temperature. The surface temperature was computed as:

$$T_S = T_I * C + T_W * (1-C) \tag{3.4-4}$$

Sensor perturbations were added as a precision error of 0.378 K and an accuracy error of 0.278 K. The resulting images are illustrated in Figure 5.

(a)   **(b)**   **(c)**   **(d)**
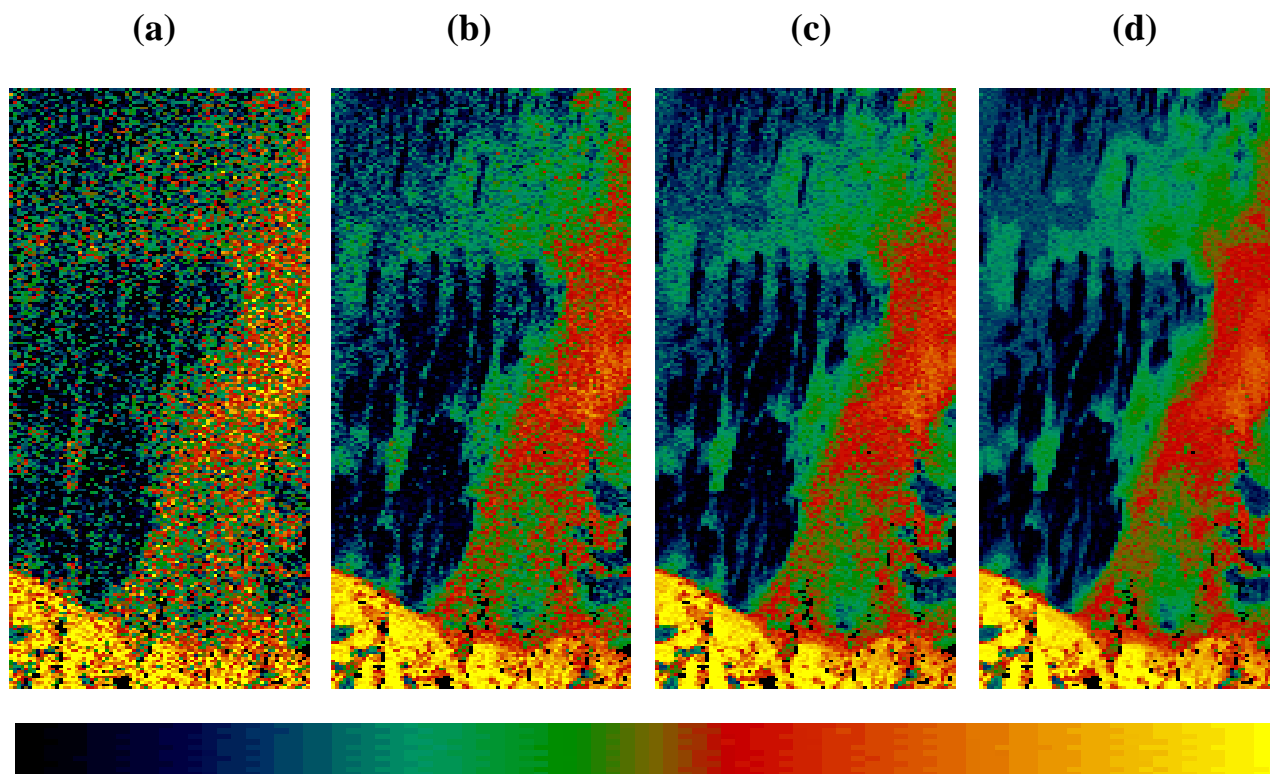
Figure 5.   Simulated VIIRS nighttime imagery of the Bering Sea scene AK74_14, for air temperatures of 0 degrees Celsius (a), -5 degrees Celsius (b), -10 degrees Celsius (c), and -20 degrees Celsius (d).

Figure 5 shows how lower air temperatures increase the thermal contrast between ice and open water, resulting in smaller ice concentration measurement uncertainty. We will specify nighttime performance for the –5 and –10 cases.

The process was repeated for a fresh water ice scene, the Lake Superior MAS scene WIN46_16. In this case, the water temperature was set to the fresh water freezing point, ice thickness was calculated, and ice temperatures calculated for air temperatures of 0, -5, -10, and –20 Celsius.

Simulations were performed at for a VIIRS nadir view and for a VIIRS edge of scan view. The simulated thermal imagery is illustrated in Figures 6 (nadir) and 7 (edge of scan).

(a)   **(b)**   **(c)**   **(d)**

Figure 6. Simulated VIIRS nighttime imagery of the Lake Superior scene WIN46_16, for air temperatures of 0 degrees Celsius (a), -5 degrees Celsius (b), -10 degrees Celsius (c), and -20 degrees Celsius (d). The imagery is simulated for a VIIRS nadir view, with Surface Temperature IP system errors added. The black pixels are land masked.

(a)   **(b)**   **(c)**
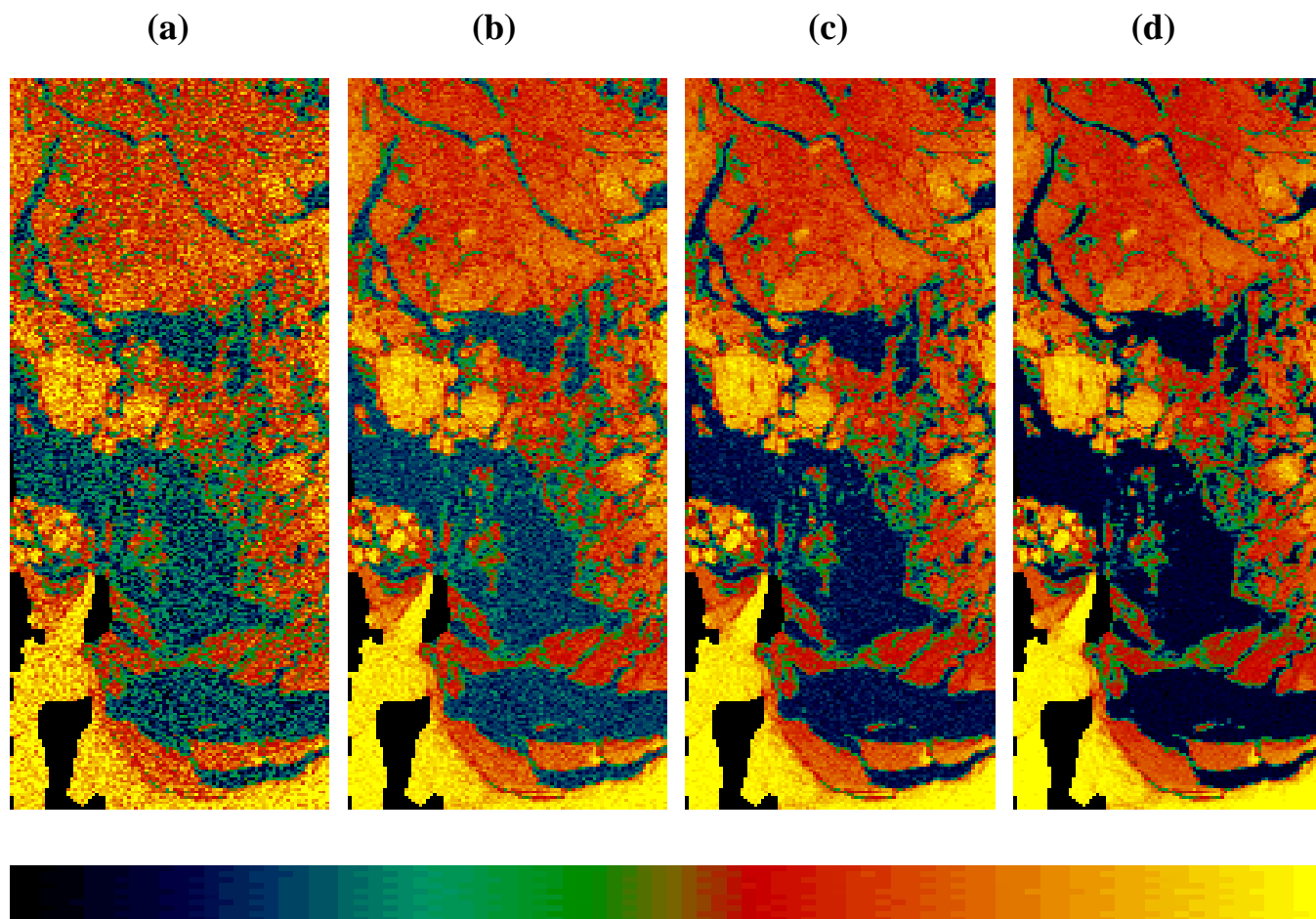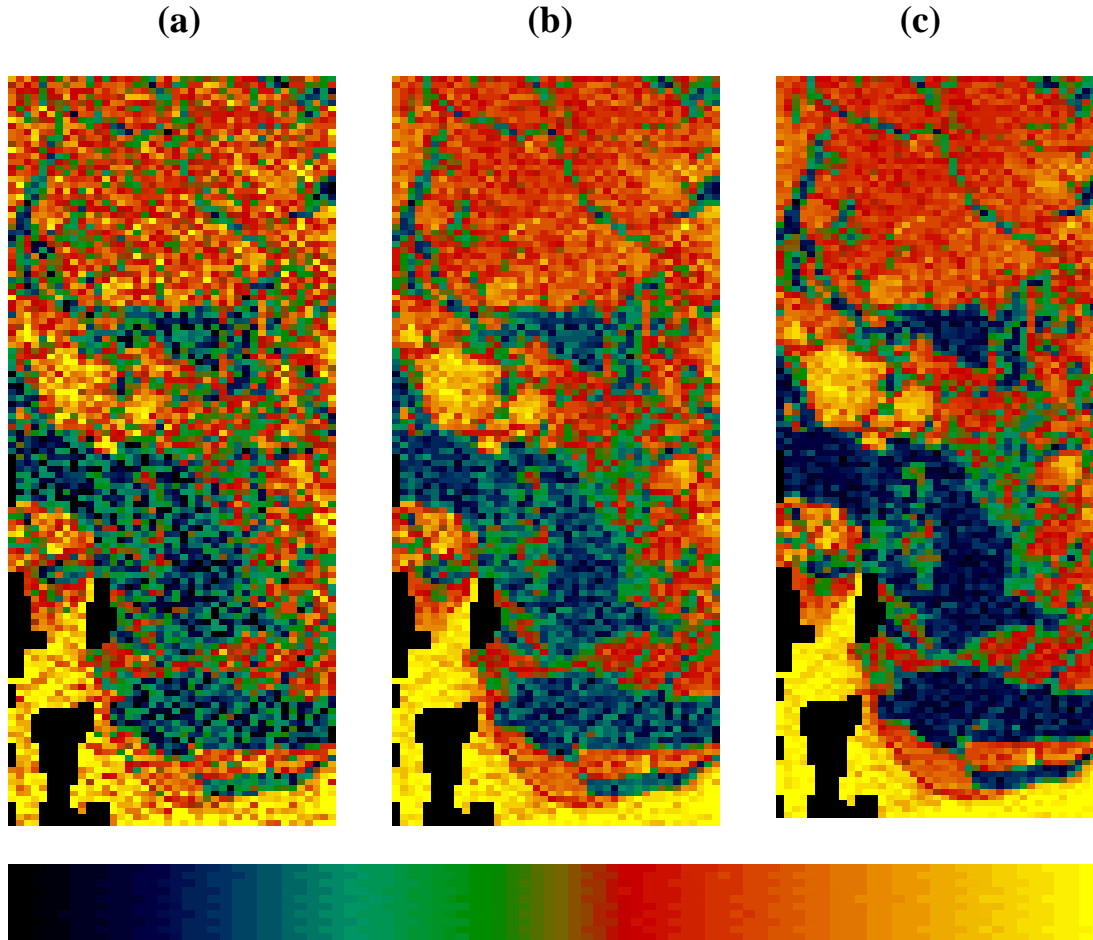

Figure 7. Simulated VIIRS nighttime imagery of the Lake Superior scene WIN46_16, for air temperatures of 0 degrees Celsius (a), -5 degrees Celsius (b), and -10 degrees Celsius (c). The imagery is simulated for a VIIRS edge of scan view, with Surface Temperature IP system errors added. The black pixels are land masked.

Measurement uncertainties were computed from the scenes for each stratification of ice concentration truth. To assign these measurement uncertainties to an ice type bin, the mean tie point difference for each truth bin was computed. The truth / type bin error was then derived as:

$$\sigma_{mn} = \sigma_m (I\text{-}W) / (I\text{-}W)_n \tag{3.4-5}$$

where: σ_{mn} = measurement uncertainty for (truth,type) bin (m,n)

σ_m = observed measurement uncertainty for truth bin (m = 1,4)

$(I\text{-}W)$ = observed mean difference in ice/water tie points

$(I\text{-}W)_n$ = mean difference in ice/water tie points for ice type (n = 1,2)

and the scaling factor (1 / (I-W)) is based on equation 3.4-2.

Tables 5, 6, 7, 8, and 9 show the errors stratified by ice concentration and ice type. The errors are for horizontal cells of 0.8 km at nadir and 3.2 km at edge of scan, under clear conditions. The third row of each table is derived as a weighted mean of the first two rows to represent a typical distribution of lake ice thickness.

Table 5. Fresh Water Ice Concentration Measurement Uncertainty,
Case 1 (Clear, Nadir, SZA=60 degrees)

	Ice Concentration Truth			
Ice Type	0.00 – 0.35	0.35 – 0.65	0.65 – 0.85	0.85 – 1.00
Young	.0537	.0755	.0769	.0844
First-Year/Multi-Year	.0265	.0373	.0380	.0417
Typical Scene	.0495	.0696	.0709	.0777

Table 6. Fresh Water Ice Concentration Measurement Uncertainty,
Case 2 (Clear, Nadir, Night, Air temperature = -5 Celsius)

	Ice Concentration Truth			
Ice Type	0.00 – 0.35	0.35 – 0.65	0.65 – 0.85	0.85 – 1.00
Young	.0359	.0730	.0663	.0662
First-Year/Multi-Year	.0277	.0563	.0511	.0510
Typical Scene	.0344	.0700	.0636	.0635

Table 7. Fresh Water Ice Concentration Measurement Uncertainty,
Case 3 (Clear, Nadir, Night, Air temperature = -10 Celsius)

	Ice Concentration Truth			
Ice Type	0.00 – 0.35	0.35 – 0.65	0.65 – 0.85	0.85 – 1.00
Young	.0331	.0672	.0611	.0610
First-Year/Multi-Year	.0255	.0518	.0471	.0470
Typical Scene	.0317	.0644	.0586	.0585

Table 8. Fresh Water Ice Concentration Measurement Uncertainty,
Case 4 (Clear, Edge of Scan, SZA = 60 degrees)

	Ice Concentration Truth			
Ice Type	0.00 – 0.35	0.35 – 0.65	0.65 – 0.85	0.85 – 1.00
Young	.0642	.0996	.0874	.0724
First-Year/Multi-Year	.0317	.0492	.0432	.0358
Typical Scene	.0592	.0917	.0806	.0667

Table 9. Fresh Water Ice Concentration Measurement Uncertainty,
Case 5 (Clear, Edge of Scan, Night, Air temperature = -5 Celsius)

Ice Type	Ice Concentration Truth			
	0.00 – 0.35	0.35 – 0.65	0.65 – 0.85	0.85 – 1.00
Young	.0350	.0956	.0707	.0547
First-Year/Multi-Year	.0270	.0737	.0545	.0422
Typical Scene	.0335	.0916	.0678	.0525

It should be noted that the $(1 / (I\text{-}W))$ factor in the equation for ice concentration measurement uncertainty is the primary determinant of performance. As the contrast between ice and water $(I\text{-}W)$ decreases, errors increase inversely. Our simulations indicate that we do not attain our specification when the thermal contrast between ice and water is less than 2.2 K and the visible reflectance contrast is less than 0.14. The effect of reducing all of our system errors by a factor of 2, for example, would allow us to attain our specification for an additional range of 1.1 K in ice temperature. Performance is limited more by the geophysical conditions of the scene than by the sensor/algorithm limitations.

3.4.2.2 Ice Edge Boundary

Ice edge boundary is computed by linear interpolation of the measured ice concentrations between neighboring pixels. Neighboring pixel pairs are selected when their measured concentrations are on different sides of the 0.1 concentration threshold defining an ice edge.

$$\text{Lat} = (\ (C_1 - 0.1) \times (\text{Lat})_2 + (0.1 - C_2) \times (\text{Lat})_1\ ) / (C_1 - C_2) \tag{3.4-6}$$

where: C_1 = measured ice concentration for pixel with greater concentration

     $(\text{Lat})_1$ = latitude for pixel with greater concentration

     C_2 = measured ice concentration for pixel with lesser concentration

     $(\text{Lat})_2$ = latitude for pixel with lesser concentration

A similar equation is applied for edge longitude.

Errors in C_1, C_2, $(\text{Lat})_1$, $(\text{Lon})_1$, $(\text{Lat})_2$, and $(\text{Lon})_2$ contribute to the measurement uncertainty:

$$\sigma^2_{\text{Lat}} = (A\ ((\text{Lat})_1 - (\text{Lat})_2)^2\ \sigma^2_C\ ) / (C_1 - C_2)^2\ )\ +\ \sigma^2_G \tag{3.4-7}$$

where: A   = factor depending on separation of C1 and C2 from 0.1.

     σ_G = Geo-location error in latitude.

and σ^2_C $= \sigma^2_{C1} = \sigma^2_{C2}$ is assumed.

Raytheon

A similar equation applies to longitude error.

The combined edge location error therefore has the form:

$$\sigma^2_{Edge} = \quad B \ P^2 \ \sigma^2_C \ + \ \sigma^2_G \tag{3.4-8}$$

where : P = separation of pixel centers (km)

σ_G = Geo-location error of the pixel centers (km)

and:

$$B = A / (C_1 - C_2)^2 \tag{3.4-9}$$

Our analysis of ice edge boundary measurement uncertainty was performed as follows:

We applied our algorithm to the same MODIS Airborne Simulator (MAS) scenes we used for ice concentrastion (c.f. Section 3.6.2.1) at a 50 meter pixel resolution. Reflectances in MAS bands 3 (648 nm) and 7 (866 nm) were calculated from the TOA radiances. Brightness temperatures in MAS bands 45 (11 μm) and 46 (12 μm) were calculated from the TOA radiances. Surface temperature was computed by the Ice Surface Temperature algorithm. The surface reflectances and surface temperature were used as input data for our algorithm. Our ice concentration algorithm was applied. The retrieved ice concentration was used as input data to our ice edge algorithm. The latitude/longitude coordinates for compact edges were adopted as edge boundary "truth".

We applied the ice concentration algorithm to the perturbed VIIRS scenes. The retrieved ice concentration was used as input data to our ice edge algorithm. We calculated the distance between each retrieved compact ice edge boundary location and the nearest "true" ice edge, converting degrees latitude and longitude to km. The conversion accounts for the cosine of the latitude reduction in longitude degree to km conversion.

An example is shown as Figure 8.
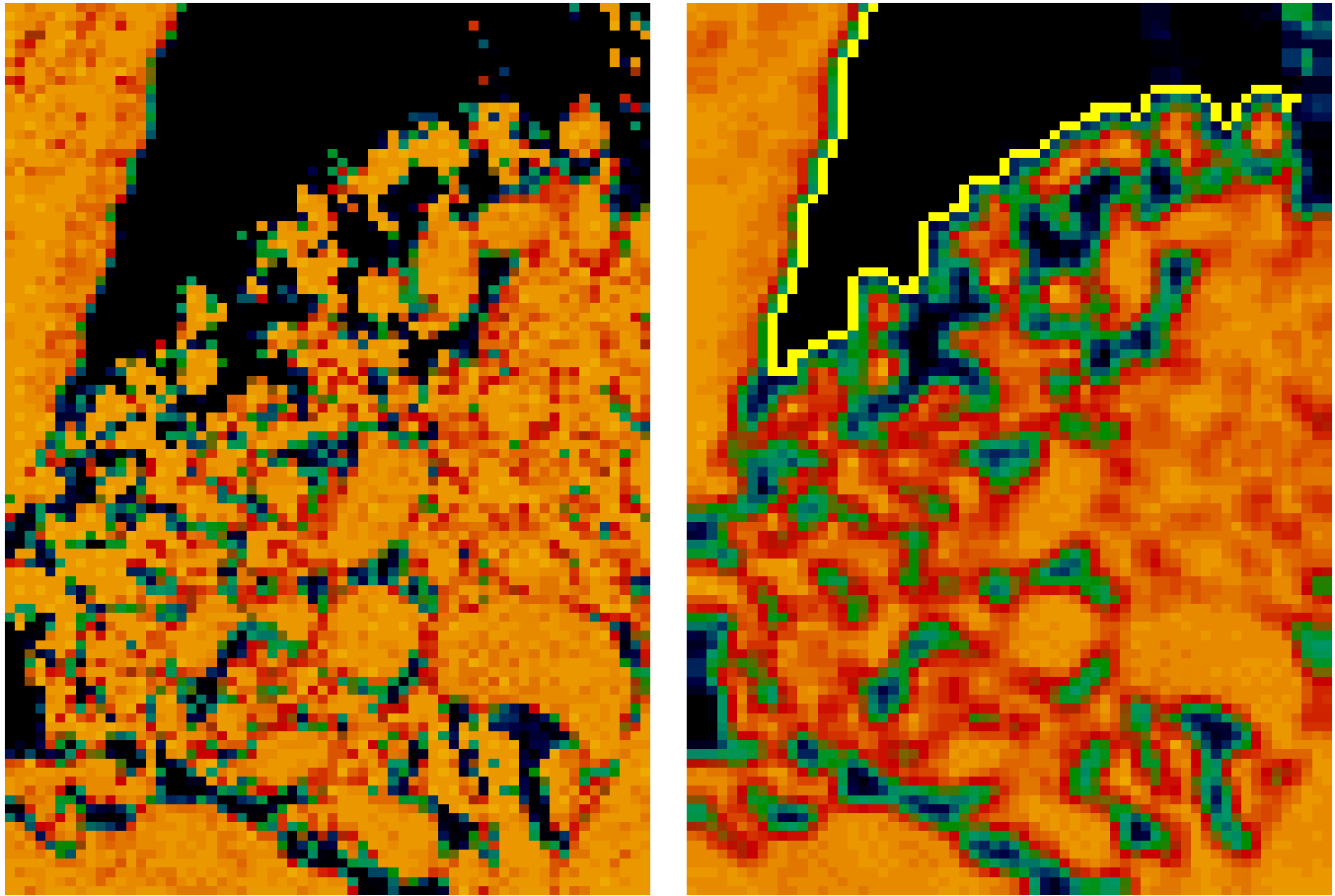
Figure 8. Illustration of ice edge boundary retrieval.

The scene is from the FIRE-ACE campaign of the MODIS Airborne Simulator (ACE_65_3). The ice concentration retrieval at nadir (left) is input to the algorithm, which produces compact and diffuse ice edge isolines (right). The isolines are superimposed on the smoothed ice concentration map used by the algorithm to derive diffuse ice edge boundary location.

The algorithm output is also a set of latitude/longitude coordinates, derived in the vicinity of the isolines by equation 3.4-1. Ice edge boundary measurement uncertainty is calculated from the deviation of the retrieved edge coordinates from the coordinates of the nearest true ice edge. The mean boundary location error for the compact edge is 0.134 km.

The error is assumed to scale with ice concentration measurement error, from equation 3.4-3. We therefore scaled our derived edge boundary measurement errors by the corresponding ice concentration measurement uncertainties for the different ice types, as indicated in Section 3.4.2.1. That is, we use the observed errors in ice concentration and ice edge boundary to determine the B factor for the scene, which we adopt as typical for a compact ice edge.

Geo-location errors of 0.067 km at nadir and 0.233 km at edge of scan were then applied, following our system specification for geo-location error *[SS154640-001]*.

Tables 10, 11, and 12 show the errors stratified by scan angle and ice type. The third row of each table is derived as a weighted mean of the first two rows to represent a typical distribution of lake ice thickness. The errors apply to compact ice edges only. Errors for diffuse ice edges will depend on the spatial scale of ice concentration gradient.

**Table 10. Ice Edge Boundary Measurement Uncertainty (km),
Case 1 (Clear, SZA=60 degrees)**

Ice Type	Scan Angle	
	Nadir	Edge of Scan
Young	0.266	0.690
First-Year/Multi-Year	0.144	0.396
Typical Scene	0.246	0.642

**Table 11. Ice Edge Boundary Measurement Uncertainty (km),
Case 2 (Clear, Night, Air Temperature = -5 Celsius)**

Ice Type	Scan Angle	
	Nadir	Edge of Scan
Young	0.247	0.672
First-Year/Multi-Year	0.195	0.539
Typical Scene	0.237	0.647

**Table 12. Ice Edge Boundary Measurement Uncertainty (km),
Case 3 (Clear, Night, Air Temperature = -10 Celsius)**

Ice Type	Scan Angle	
	Nadir	Edge of Scan
Young	0.210	0.610
First-Year/Multi-Year	0.167	0.493
Typical Scene	0.202	0.588

Typical performances at nadir are better than 0.3 km, compared with our specification of 0.4 km.

Typical performances at edge of scan are better than 0.7 km, compared with our specification of 1.0 km.

As ice edge boundary is derived from ice concentration, the error is similarly sensitive to the contrast between ice and water.

3.4.3 Error Budgets

We identify the following factors as possibly contributing to the total error budget for ice concentration:

- Tie Point errors
- Sensor noise
- Calibration
- MTF
- Band Registration

Tie Point Errors: The real variation in ice and water tie points can not be entirely accounted for with a data set of finite spatial resolution. We model these errors by comparing the retrieval of ice concentration at VIIRS resolution with the retrieval at MAS resolution. We make the reasonable assumption that the tie point errors at a resolution of 50 meters are negligible compared with the errors at a resolution of 0.4 km.

Sensor Noise: The dominant source of error in measured reflectance and/or temperature is expected to be the precision error. This error is due to sensor noise and to variations in atmospheric condition on the spatial scale of the VIIRS pixel. Our analysis shows that sensor noise will be the dominant precision error for most cases. We therefore model these errors by perturbing our "true" reflectances and temperatures by adding sensor noise to the radiances.

Calibration: Our algorithm is not expected to be sensitive to accuracy errors in reflectance and temperature, since the measured parameter, the ice tie point, and the water tie point will all be shifted by the same error. To test this hypothesis, we applied a calibration bias of 2% to the reflectance and 0.5% to the temperature.

MTF: MTF smearing of the radiances will alias real horizontal variability into errors in measured reflectance and/or temperature for a given pixel. We model these errors on our scenes by applying the sensor MTF specification to the images.

Band Registration: Band-to-band registration errors will also alias horizontal variability into measurement error. These errors only apply to a retrieval which uses more than one band. Since our performance analysis is based on single band retrieval, band registration errors were not simulated. If the retrieval were to use more than one band to enhance performance, band registration error must be considered. For now, we note that the current performance analysis can always be achieved with a single band. If a multi-band result is worse, due to the effects of band registration or non-optimum band weighting, we always have the option of using the single band.

An error budget for ice concentration is shown in Table 13.

Raytheon

Table 13. Error Budget for Fresh Water Ice Concentration

FRESH WATER ICE CONCENTRATION Specification v3 (PDR)	Case:	Clear, Nadir, SZA = 60 degrees, Truth = 0.85-1.0, Typical Scene
	Measurement Uncertainty (km)	Reference
Threshold	TBD	VIIRS SRD
Objective	TBD	VIIRS SRD
System Specification	0.1	Raytheon VIIRS Specification v3
System Performance	0.0777	This document, Section 3.4.2.1
System Margin	0.0630	RSS Difference of Specification and Performance
Algorithm Performance	0.0732	This document, Section 3.4.2.1
Sensor Performance	0.0261	This document, Section 3.4.2.1

We identify the following factors as contributing to the total error budget for ice edge boundary:

- Ice Concentration
- Horizontal Spatial Resolution (HSR)
- Geo-location

Ice Concentration: The algorithm uses the ice concentration image as input data. Errors in ice concentration will result in ice edge boundary measurement error, as can be seen from Equation 3.4-8. We model these errors by comparing ice edge boundary retrievals from "true" ice concentration with retrievals from ice concentration perturbed by our various error models, as described in Section 3.4.2.1.

Horizontal Spatial Resolution: The coarseness of the VIIRS pixel size (P in equation 3.4-8) will limit the accuracy of the interpolation of pixelized ice concentration to ice edge coordinates.

Geo-location: Errors in geo-location of the VIIRS reflectances and temperatures input to the ice concentration algorithm will propagate into error in the ice edge boundary derived from ice concentration.

The B factor in equation 3.4-8 is scene dependent, and depends on the compactness of the ice edge. Our errors are derived from analysis of compact edges only. The error due to non-zero P combines with the ice concentration error, so is not budgeted separately. The combined pixel resolution/ice concentration error is budgeted as "ice concentration/resolution". The error is allocated to the algorithm subsystem, as the ice concentration algorithm error is larger than the ice concentration sensor error.

Error budgets for ice edge boundary are shown in Tables 14 and 15.

Table 14. Error Budget for Fresh Water Ice Edge Boundary

FRESH WATER ICE EDGE BOUNDARY	Case:	Clear, Night, Air Temperature = -5 Celsius, Nadir, Typical Scene
Specification v3 (PDR)		
	Measurement Uncertainty (km)	Reference
Threshold	TBD	VIIRS SRD
Objective	TBD	VIIRS SRD
System Specification	0.400	Raytheon VIIRS Specification v3
System Performance	0.237	This document, Section 3.4.2.2
System Margin	0.322	RSS Difference of Specification and Performance
Concentration / Resolution	0.228	This document, Section 3.4.2.2
Geo-location	0.067	Raytheon VIIRS Specification v3

Table 15. Error Budget for Fresh Water Ice Edge Boundary

FRESH WATER ICE EDGE BOUNDARY	Case:	Clear, Night, Air Temperature = -5 Celsius, Edge of Scan, Typical Scene
Specification v3 (PDR)		
	Measurement Uncertainty (km)	Reference
Threshold	TBD	VIIRS SRD
Objective	TBD	VIIRS SRD
System Specification	1.000	Raytheon VIIRS Specification v3
System Performance	0.647	This document, Section 3.4.2.2
System Margin	0.762	RSS Difference of Specification and Performance
Concentration / Resolution	0.604	This document, Section 3.4.2.2
Geo-location	0.233	Raytheon VIIRS Specification v3

3.4.4 Limits of Applicability

In this section, we discuss the conditions under which our specified performance can not be attained.

Cloudy: The Fresh Water Ice EDR is required under clear conditions only, with clear defined as a cloud optical thickness less than 0.03. Our specification is for clear scenes only. The standard approach to minimize errors caused by clouds is to mask pixels where clouds are likely to be present in the radiance path. The VIIRS Cloud Mask *[V-29]* will perform this function. Because no cloud mask is perfect, there will be some source of error caused by the effects of unmasked clouds. Thin clouds will perturb the upwelling surface radiance by absorption and scattering, and will also be a source of reflected radiance unrelated to the surface. There will also be error due to incorrect classification of cloud contaminated pixels as clear. There will also be effects from

cloud shadows. Cloud error assessment will require an analysis of cloud masking performance over ice surfaces. It is desirable to perform tests to determine the expected size of the retrieval errors under various conditions of cloud optical thickness and phase. Thin cirrus clouds are a particularly important case of cloud error, because they are particularly difficult for the cloud mask to detect over snow. These tests require the simulation of TOA radiances from snow surfaces with a variety of overlying cloud layers. In the absence of these tests, we cannot quantify the effect of clouds. The conditions under which the specification can not be attained may include a range of cloud optical thickness. The range will be determined by a balance between the increasing effect of clouds on the signal and the increasing probability of correct masking. The specification of this range has been deferred to future verification activity. It is expected that the VIIRS Cloud Mask, which will build on MODIS heritage and experience, will perform well enough to allow for effective operational retrieval of lake ice data from VIIRS.

Low Contrast Between Ice and Water Tie Points: The error in ice concentration scales inversely with the difference between the ice and water tie points. As this difference approaches a critical point, performance degrades rapidly. Our simulations indicate that we do not attain our specification for ice concentration measurement uncertainty when the thermal contrast between ice and water is less than 2.2K and when the reflectance differences are less than 0.14. In general, we will then not attain our specification for ice edge boundary measurement uncertainty. This occurs under the following conditions:

Warm Nights: The thermal contrast between ice and open water may be too low when surface air temperature is warmer than –5 Celsius. This condition can occur during warm winter nights.

Twilight of Warm Days: A reliance on solar reflectance bands suffers from limitations during low light conditions. If it is a warm day, thermal contrast between ice and water will be too low to allow good performance from temperature data.

"New" ice: Temperature and reflectance contrasts are strongly dependent on ice thickness. The contrasts are generally too low for ice with a thickness less than 0.05 to 0.1 meters, depending upon local conditions. Our specification and performance result therefore excludes "New" ice.

3.5   PRACTICAL CONSIDERATIONS

3.5.1   Numerical Computation Considerations

We optimized our scheme of choosing parameters in sliding window. As a result of this improvement, the requirement to retrieve ice products on a global, operational basis in a 20 minute time frame places no constraints on our algorithms.

3.5.2   Programming and Procedural Considerations

All procedures are automatic, to perform in the operational environment.

3.5.3   Configuration of Retrievals

The Fresh Water Ice algorithm expects the VIIRS Cloud Mask IP, the VIIRS Surface Reflectance IP, and the VIIRS Ice Surface Temperature IP. The NPOESS processing configuration is designed to satisfy these expectations.

3.5.4 Quality Assessment and Diagnostics

Quality flags will be attached to each archived result.

3.5.5 Exception Handling

Pixels identified by the cloud mask will be skipped. Pixels with bad quality flags will be skipped and flagged. Bands with bad quality flags will be removed.

3.6 INITIALIZATION AND VALIDATION

Initialization and validation activities shall be coordinated with the National Ice Center, with the purpose of assuring that the VIIRS data products can be incorporated into their strategic product. MODIS Airborne Simulator (MAS) observations will be used to optimize cloud detection over ice surfaces. The VIIRS Cloud Mask will be applied over a series of MAS images for which there are varying types of ice to evaluate and optimize its performance.

Detection of shadows over ice covered regions will be investigated to initially flag the pixels where shadows exist. In the case of a shadow being detected the effects of the shadows need to be assessed. In the polar regions cloud shadows are quite common due to both the frequency of cloud cover, and the low sun angles. Shadows are seen as a risk which may be reduced by using both radiative transfer modeling and analyzing MAS data in which shadows are visible over snow covered regions.

Radiative transfer models will be applied to large solar zenith angle data to optimize the models for polar conditions, and to develop decision rules for solar zenith angle thresholds. MODIS data taken at solar zenith angles greater than 70 degrees will be studied to fine tune our solar zenith angle threshold for daytime conditions. The limiting factor is believed to be the reliability of atmospheric correction at larger solar zenith angles. Plane parallel radiative transfer algorithms are inaccurate for angles greater than 70-75 degrees. Development of improved radiative transfer models at larger angles will allow us to relax this constraint. To solve the Radiative Transfer Equation appropriately one would have to take into account the spherical shell atmosphere geometry (Thomas and Stamnes, 1998). It is expected that "truth" can be established from *in situ* data obtained from MODIS validation campaigns.

The plan includes sensitivity studies, analysis of simulated VIIRS data, and verification using MODIS-type data. Observations from AVIRIS, MAS, MODIS, GLI, and NPP will be used in the pre-launch phase to study the error characteristics and optimum techniques for the algorithm. It is expected that post-launch MODIS validation data will be of great value. This data is expected to include *in situ* field measurements combined with MODIS observations, MAS underflights, and low level aircraft measurements at spatial resolutions less than 10 meters. Our plan is to use this data in combination with the VIIRS sensor model to produce simulated VIIRS scenes, apply our algorithms to retrieve our ARPs, and compare our results with "truth" derived from *in situ*, aircraft, and MAS data.

Band weights will be selected during pre-launch characterization, using MODIS validation data. These weights may be seasonal, as the reflectance and thermal contrasts between ice and open water vary seasonally. The optimum weights of the 645 nm and 865 nm bands will be

determined by comparison of simulated VIIRS retrievals to ground truth from MODIS validation data.

Our plan is designed to interface smoothly with post-launch validation activity. We would propose to conduct a post-launch VIIRS validation campaign similar to the MODIS validation activity. In this sense, post-launch validation will already have been simulated by the pre-launch validation activity. Following launch, we would substitute real VIIRS data for the pre-launch simulated data. We would establish "truth" by the same process.

4.0   ASSUMPTIONS AND LIMITATIONS

4.1   ASSUMPTIONS

The following assumptions apply to the algorithms described in this document:

- An effective cloud mask over snow and ice surfaces will be available from the VIIRS Cloud Mask IP *[Y2412]*.

- Surface reflectances, brought to standard conditions, will be derived from TOA radiances with errors as specified in the VIIRS System Specification *[SS154640-001]*.

- A Surface Temperature IP will be provided, with errors as specified in the VIIRS System Specification *[SS154640-001]*.

4.2   LIMITATIONS

The following limitations apply to the algorithms described in this document:

- Clear conditions only. The definition of "clear" will be developed in coordination with the development of the VIIRS Cloud Mask IP *[Y2412]*. It will depend upon the capability of the cloud mask over snow and ice surfaces and upon the capability of radiative transfer modeling through thin clouds.

5.0   REFERENCES

Ackerman, S. *et al,* (1997). Discriminating clear sky from cloud with MODIS. ATBD-MOD-06. http://eospso.gsfc.nasa.gov/atbd/modistables.html

Assel, R.A. (1990). An ice cover climatology for Lake Erie and Lake Superior for the winter seasons 1897-1898 to 1982-1983. *Intl. J. of Climate,* 10, 731-748.

Bohren, C.F., and B.R. Barkstrom (1974). Theory of the optical properties of snow. *J. Geophys. Res.*, 79, 4527-4535.

Bolsenga, S.J. (1977). Preliminary observations of the daily variation of ice albedo. *J. Glaciology,* 18(80), 517-521.

Bolsenga, S.J. (1983). Spectral reflectances of snow and fresh-water ice from 340 through 1100 nm. *J. Glaciology,* 29(102), 296-305.

Crane, R.G., and M.R. Anderson (1984). Satellite discrimination of snow/cloud surfaces. *Intl. J. Remote Sens.*, 5(1), 213-223.

Dozier, J. (1984). Snow reflectance from Landsat-4 Thematic Mapper. *IEEE Trans. Geosci. Remote Sens.*, 22(3), 323-328.

Dozier, J. (1998). Spectral signature of alpine snow cover from the Landsat Thematic Mapper. *Remote Sens. Environ.*, 28, 9-22.

Eppler, D.T., L.D. Farmer, A.W. Lohanick *et al.* (1992). Passive microwave signatures of sea ice. In Micowave Remote Sensing, of Sea Ice, Geophysical Monograph 68, American Geophysical Union, 47-71.

Grenfell, T.C., and G.A. Maykutt (1977). The optical properties of ice and snow in the Arctic Basin. *J. Glaciology,* 18(80), 445-463.

Grenfell, T.C., and D.K. Perovich (1984). Spectral albedos of sea ice and incident solar irradiance in the southern Beaufort Sea. *J. Geophys.Res.,* 89(C3), 3573-3580.

Grenfell, T.C., D.K. Perovich, and J.A. Ogren (1981). Spectral albedos of an alpine snowpack. *Cold Regions Sci. Technol.*, 4, 121-127.

Hall, D.K., A. Tait, G. Riggs, and V. Salomonson, (1998). MODIS: Snow mapping algorithm and the sea ice mapping algorithm. 1998 (Version 4.0). ATBD-MOD-10. http://eospso.gsfc.nasa.gov/atbd/modistables.html

Hall, D.K., J.L. Foster, A.T.C. Chang, and A. Rango (1981). Freshwater ice thickness observations using passive microwave sensors. *IEEE Trans. Geosci. Remote Sens.*, GE-19(4), 189-193.

Hall, D.K., G.A. Riggs, and V.V. Salomonson (1995). Development of methods for mapping global snow cover using MODIS data. *Remote Sens. Environ.*, 54, 127-140.

Jeffries, M.O., K. Morris, and W.F. Weeks (1994). Structural and stratigraphic features and ERS-1 synthetic aperture radar backscatter characteristics of ice growing on shallow lakes in NW Alaska, winter 1991-1992. *J. Geophys. Res.,* 99(C11), 22,459-22,471.

Leshkevich, G. A. (1981). Categorization of northern Green Bay ice cover using Landsat-1 digital data – a case study. NOAA Technical Memorandum ERL GLERL-33, National Technical Information Service, Springfield, VA, 19 pp.

Leshkevich, G.A. (1985). Machine classification of freshwater ice types from Landsat-1 digital data using ice albedos as training sets. *Remote Sens. Environ.,* 17(3), 251-263.

Leshkevich, G.A. (1995). Satellite mapping of Great Lakes ice cover. in *First MODIS Snow and Ice Workshop,* D.K. Hall, ed., NASA Conference Publication 3318, pp. 87-91.

Mannen, J. T. (1996). Cost and Operational Benefits Requirements Analysis Report (COBRA), NPOESS Integrated Program Office, June 12, 1996.

Massom, R., and J.C. Comiso (1994). The classification of Arctic sea ice types and the determination of surface temperature using AVHRR data. *J. Geophys. Res.,* 99(C3), 5201-5218.

Melloh, R.A., D.T. Eppler, L.D. Farmer, L.W. Gatto, and E.F. Chaco (1981). *Interpretation of passive microwave imagery of surface snow and ice, Harding Lake, Alaska,* CRREL Report 91-11, Cold Regions Research and Engineering Laboratory, Hanover, NH.

Morris, K., M.O. Jeffries, and W.F. Weeks (1995). Ice processes and growth history on Arctic and sub-Arctic lakes using ERS-1 SAR data. *Polar Record,* 31(177), 115-128.

Rondy, D.R. (1976). Great Lakes ice cover. In *Limnology of lakes and embayments*, *Great Lakes Basin framework study,* Appendix 4, Ann Arbor, Great Lakes Basin Commission, pp. 105-117.

Schertler, R.J., R.A. Mueller, R.J. Jirberg *et al.* (1975). Great Lakes all-weather ice information system. *NASA Technical Memorandum NASA TM X-71815,* National Technical Information Service, Springfield, VA,22161, 13 pp. and 16 pp. of figures.

Swift, C.T., R.F. Harrington, and H.F. Thornton (1980). Airborne microwave remote sensing of lake ice. *Proceedings of EASCON'80 Conference,* IEEE, New York, pp. 369-373,

Swift, C.T., W.L. Jones, R.F. Harrington *et al*. (1980). Microwave radar and radiometric remote sensing of lake ice. *Geophysical Research Letters,* 7, 243-246.

Thomas, G., and K. Stamnes (1998). Radiative transfer in the atmosphere and ocean. Textbook, Cambridge Atmospheric and Space Sciences Series.

Warren, S.G. (1982). Optical properties of snow. *Rev. Geophys. Space Phys.*, 20(1), 67-89.

Wiesnet, D.R. (1979). Satellite studies of fresh water ice movement on Lake Erie. *J. Glaciology,* 24(90), 415-426.

Wiscombe, W.J., and S.G. Warren (1980). A model for the spectral albedo of snow,1, pure snow. *J. Atmos. Sci.,* 37(12), 2712-2733.